Cooling requirements for the freeze plug module

by

David Kamp

to obtain the degree of Bachelor of Science
at the Delft University of Technology,
to be defended publicly on Friday January X, 2018 at 10:30 AM.

Student number:	4307291	
Project duration:	September 25, 2017 – January X, 2018	
Thesis committee:	Dr. ir. M. Rohde,	TU Delft, supervisor
	(Prof. dr. ir. J. L. Kloosterman,	TU Delft)

TU Delft

Abstract

Never before was the quest for sustainable energy more eminent than in current times. The Thorium based Molten Salt Fast Reactor (MSFR) holds the future potential to fulfil part of the ever increasing energy demand in a sustainable way. In spite of its promise, the safety of all nuclear energy evokes more controversy in society than any other energy production method. To combat this and because of the 2011 accident with the Fukushima-Daiichi power plant, a myriad of new safety requirements for the coming generation of reactors has emerged, among which is the requirement for a passive protection system. In the MSFR development, the passive safety system consists of the freeze plug module, an actively cooled blockage which prevents the fuel salt from flowing through the draining pipes. In case of an emergency, the active cooling is cut off and the blockage melts, allowing for the fuel salt to be safety drained to underground tanks.

This thesis aims to capture the cooling requirements for a suitable freeze plug module under normal operating conditions of the MSFR. To simulate the normal operating conditions, both the molten salt LiF-ThF_4 flow and the heat transfer are modelled in COMSOL. This way, the freeze plug module influence on the molten salt flow, and vice versa, can be investigated. The molten salt flow turns out to be in the turbulent regime, with a Reynolds number of 196000. Two turbulence models, $k - \epsilon$ and Algebraic yPlus, were used to model the molten salt flow. The Algebraic yPlus model turns out to produce the more accurate results, as it does not use wall functions. The cooling requirements were investigated by exploring the influence of the volumetric cooling power and the plug module geometry. For a volumetric cooling power of 1.8 MW/m^3, a total cooling power of 10.9 kW is necessary to cool the plug so that 95% of the freeze plugs is in its solid state. It was shown that with higher volumetric cooling power, the plug is cooled more efficiently which leads to bigger freeze plugs diameters and a lower total cooling power. The resulting values for the total cooling power required are desirable in the sense that they amount to less than 0.02% of the assumed total energy capacity of the MSFR.

Contents

Abstract ii

List of Figures iv

List of Tables vi

1 Introduction 1
- 1.1 The Molten Salt Fast Reactor . . . 2
- 1.2 Fukushima-Daiichi 2011 . . . 3
- 1.3 The freeze plug . . . 3
- 1.4 Previous research . . . 3
- 1.5 Research goals . . . 5
- 1.6 Thesis outline . . . 5

2 Theoretical framework 6
- 2.1 Molten salt flow in the MSFR . . . 6
  - 2.1.1 Current design of the MSFR . . . 7
  - 2.1.2 Flow characteristics in the MSFR . . . 8
- 2.2 Turbulence modelling . . . 9
  - 2.2.1 Turbulent flow regime . . . 9
  - 2.2.2 RANS approximation . . . 9
  - 2.2.3 k-ϵ turbulence model . . . 11
  - 2.2.4 Algebraic yPlus model . . . 14
  - 2.2.5 2D approximation . . . 15
- 2.3 Heat transfer . . . 16
  - 2.3.1 Heat transfer in plug domain . . . 16
  - 2.3.2 Heat transfer in molten salt domain . . . 17

3 Numerical simulation 20
- 3.1 The experimental set up . . . 20
- 3.2 The simulation method . . . 22
  - 3.2.1 Material selection . . . 22
  - 3.2.2 Physics modules . . . 23
  - 3.2.3 Boundary conditions and Initial values . . . 23
  - 3.2.4 Mesh creation . . . 25
  - 3.2.5 Computation and post-processing . . . 28
- 3.3 COMSOL models . . . 28
  - 3.3.1 Model 1a and 1b: Establishing the velocity profile . . . 29

3.3.2 Model 2a and 2b: Determination of the volumetric cooling power $P_{cooling}$ . . 29
3.3.3 Model 3a and 3b: Influence of D_{plug} on cooling requirements 29
3.3.4 Model 4a and 4b: Influence of F_{plug} on cooling requirements 29

4 Results and discussion **30**
4.1 Establishing the developed velocity profile 30
4.1.1 Model 1a: $k-\epsilon$ velocity profile 30
4.1.2 Model 1b: Algebraic yPlus velocity profile 32
4.2 Determination of the volumetric cooling power $P_{cooling}$ 33
4.2.1 Model 2a: $k-\epsilon$ cooling power 34
4.2.2 Model 2b: Algebraic yPlus volumetric cooling power 36
4.2.3 Near-wall investigation of model 2a and model 2b 38
4.3 Geometry influence on cooling requirements 41
4.3.1 Model 3a: Plug diameter influence with $k-\epsilon$ module 41
4.3.2 Model 3b: Plug diameter influence with Algebraic yPlus module 44
4.3.3 Model 4a: Adjacent plug distance influence with $k-\epsilon$ module 45
4.3.4 Model 4b: Adjacent plug distance influence with Algebraic yPlus module . . 46
4.3.5 Geometry influence on total cooling power P_{total} 47

5 Conclusions and recommendations **49**
5.1 Conclusions 49
5.2 Recommendations 50

Bibliography **51**

A Graphs **54**

B MATLAB scripts **55**
B.1 Plotting the velocity profile 55
B.2 Near-wall investigation 57
B.3 Percentage plot generation 58

C Model log **60**
C.1 COMSOL model log 60

List of Figures

1.1 Schematic overview of an MSFR [5] 2
1.2 Freeze plug design with a single plug [9]. 3
1.3 Freeze plug design featuring alloy plug module and multiple freeze plugs [9]. 4
1.4 Plug design with added cooling fins as proposed by Deurvorst [9]. 4

2.1 Model of the reactor geometry used in this thesis. Adopted from [4]. 7
2.2 Velocity distribution in current reactor design with highlighted area of interest. Adopted from [4] 8
2.3 Simplified overview of the area of interest, indicated with red frame in figure 2.2 . . 8
2.4 Velocity profile of a turbulent flow near the wall in dimensionless coordinates. Adopted from [19]. 13
2.5 Schematic representation of the first computational node selection with wall functions. 14

3.1 Parametrization of the model geometry as used in this thesis [22]. 21
3.2 Overview of the various boundaries and domains for the heat transfer module. . . . 23
3.3 Overview of the turbulent flow boundaries and domains. 24
3.5 Comparison of a physics-controlled and a user-controlled mesh configuration 25
3.6 Velocity calculations with physics-controlled meshes. 26
3.7 Velocity profile calculations with user-controlled meshes. 26
3.8 Velocity calculations with user-controlled meshes. 27

4.1 Downstream average flow velocity U in the middle of the channel at y= 0.075 m. . . 31
4.2 Developed flow velocity profile as present at L_{chann}=20 m. 31
4.3 Developed turbulence variable profiles as present at L_{chann}=20 m. 32
4.4 Downstream average flow velocity U in the middle of the channel at y=0.075 m . . . 32
4.5 Developed flow velocity profile as present at L_{chann}=5 m. 33
4.6 Temperature profiles in molten salt flow and freeze plug for different volumetric cooling powers. The unit of P is [W/m^3]. 34
4.7 Relation of percentage solid freeze plug material and $P_{cooling}$. 35
4.8 Relation of total cooling power P_{total} and solid % CsCl. 36
4.9 Temperature profiles in molten salt flow and freeze plug for different cooling powers. 36
4.10 Relation of percentage solid freeze plug material and $P_{cooling}$. 37
4.11 Relation of total cooling power P_{total} and % solid CsCl. 37
4.12 Model 2a: Temperature profiles in boundary layer and plug module. 39
4.13 Model 2b: Temperature profiles in boundary layer and plug module above Hastelloy N section. 40
4.14 Detail of the setup used for models 3a and 3b, showing the plug module and its parametrisation. 42

4.15 $k-\epsilon$ analysis on D_{plug} influence on cooling requirements. 42
4.16 D_{plug} influence on percentage solid CsCl. 43
4.17 Model 3a relation between total cooling power P_{total} and percentage solid CsCl. . . . 43
4.18 Algebraic yPlus analysis on D_{plug} influence on cooling requirements. 44
4.19 Relation of D_{plug} and percentage solid CsCl. 44
4.20 Model 3b relation between P_{total} and percentage solid CsCl. 45
4.21 Fit of F_{plug} influence on solid portion CsCl, including plug configuration measurements. 46
4.22 Fit of F_{plug} influence on solid portion CsCl, including plug configuration measurements. 46

A.1 Downstream turbulence variables in the middle of the channel at y=0.075 m 54

List of Tables

2.1 Properties of the molten salt LiF-ThF4. 6
2.2 Frequently used COMSOL turbulence models [17]. 10

3.1 Standard dimensions of the model geometry as presented in figure 3.1. N_{plugs} represents the number of plugs. 22
3.2 Some of the thermal and physical properties the materials used in the COMSOL models. 22

C.1 Overview of some of the COMSOL models. 60
C.2 Overview of COMSOL models 2 61
C.3 Overview of COMSOL models 3 61

Chapter 1

Introduction

In the face of the impact that fossil fuels have on the planet's ecosystem and their diminishing supply, the quest for sustainable and alternative energy resources was never more imminent. While the developments in and funds allocated to further developing renewable energy sources are substantial, nuclear energy holds the potential to be a suitable alternative to traditional energy sources as well.
However, no other energy source has evoked such controversy about its safety. Considering the grave and structural damage incidents at nuclear power plants could potentially bring about, strict safety standards should be kept. Nuclear waste, in particular, holds the ability to inflict severe damage to the environment it is stored in due to its radio-activity. Adding in the enormous time span for which the waste has to be safely contained due to extended half life times makes for a challenging and delicate process.
In conjunction with the former is the somewhat damaged public reputation of nuclear energy, due to incidents surrounding nuclear power plants in the past. Taking the concerns of the public into account, the Generation IV International Forum (GIF) has sparked a new generation of nuclear power plants. These Generation IV nuclear power plants are set to deal with some of the problems encountered in previous generations of nuclear plants with respect to safety, sustainability and overall efficiency and are set to be deployed between 2020 and 2030. The GIF has selected six technologies for further research and development within the Generation IV nuclear plants [1]. These include:

- Lead-cooled Fast Reactor (LFR)
- Gas-cooled Fast Reactor (GFR)
- Molten Salt Reactor (MSR)
- Super-critical Water-cooled Reactor (SCWR)
- Sodium-cooled Fast reactor (SFR)
- Very High Temperature Reactor (VHTR)

The Delft University of Technology contributes to the research of the Generation IV reactors by participating in the Safety Assessment for the Molten Salt Fast Reactor project (SAMOFAR). Alongside the Delft University of Technology, 10 other partners make up the research consortium that focuses on the development of safety mechanisms of the Molten Salt Fast Reactor. The SAMOFAR project has its focus specifically on innovative safety and waste management systems.

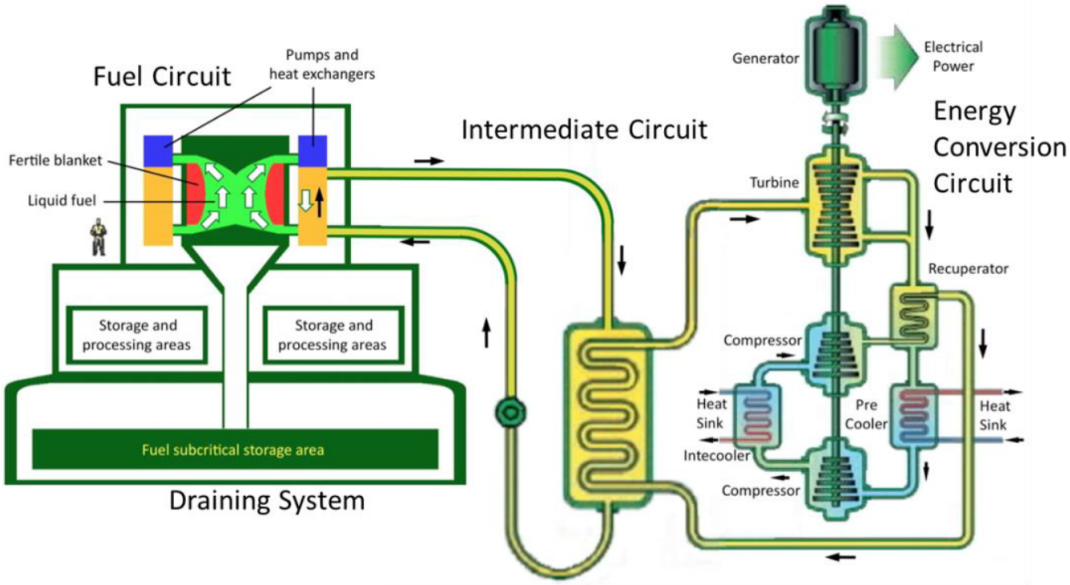

Figure 1.1: Schematic overview of an MSFR [5]

The freeze plug is one of the safety systems in development and will act as the focus of this thesis report [2].

1.1 The Molten Salt Fast Reactor

Molten Salt Reactors are a class of nuclear fissile reactors and owe their name to the fact that the fuel and coolant within the reactor vessel are molten salts. The focal point of this thesis will be centered around the Molten Salt Fast Reactor, a subclass of Molten Salt Reactors.
Within Molten Salt reactors the fissile material is dissolved in the molten fuel salt and subsequently brought into circulation. The physical properties of the salt allow the reactor to operate at high temperatures (950 K to 1000 K) and at near atmospheric pressure. Typically, Fluoride salts are used for their high thermal expansion. The high thermal expansion coefficients ensure the self regulating property of the salt, eliminating the need for solid modulator rods. The high thermal expansion dictates that in case of small perturbations in the activity of the reactor core, and thus of the temperature, the salt expands and the activity of the core decreases [3]. It is possible to use the same salt in the heat exchanger as a coolant. An schematic overview of a Molten Salt Reactor is provided in figure 1.1.
Molten Salt Fast Reactors frequently depend on the $^{233}U -^{232} Th$ fission cycle as it produces less waste that has to be contained due to its higher fuel burn-up than regular ^{235}U reactors. The MSFR makes use of the following neutron reaction:

$$^{232}Th + n \rightarrow^{233} U$$

Because the neutron is in the fast thermal spectrum, the reactor is called a Molten Salt Fast Reactor. When considering the safety of the MSFR, an advantage is the exclusion of pressure related risks due to the possibility to run operations at atmospheric pressure. The temperature of the fuel salt entering the reactor vessel is 950K and the temperature of the salt leaving the vessel is 1021K [4]. The high temperatures do pose a threat to the safety of the reactor. In case of an emergency the temperature might increase substantially.

1.2 Fukushima-Daiichi 2011

An unfortunate real display of the risks of nuclear power was experienced in the wake of the Great East Japan Earthquake at the Fukushima-Daiichi nuclear power plant in march 2011. While the plant was designed to withstand intense earthquakes, the quake did harm the regular power systems. In accordance to emergency protocols, the back up generator kicked in and the plant had sufficient power supply again. It wasn't that problems arose until the tsunami, that had been triggered by the earthquake, hit the plant, submerging the emergency back-up generator. Without energy supply both the pump to circulate the molten salt and the heat exchanger did not function adequately. Subsequently, the reactor core became separated from its heat sink and melted.
This incident has inspired an important new safety requirement for future nuclear power plant designs, namely the introduction of a passive emergency system for the draining of the decay heat in case of a power outage. In the case of the Generation IV MSFR the proposed system is a freeze plug.

1.3 The freeze plug

The freeze plug is installed in the draining pipe of the reactor vessel and relies on the fundamental process of melting. During regular operations, the plug is actively cooled, resulting in a solid constituency to prevent the molten salt from passing through the draining pipe. In case of a power outage, the cooling system of the plug stops working and the decay heat from the molten salt causes the freeze plug to melt. The material of the freeze plug is CsCl [6], which is a solid at the operating temperature of around 950K. During normal operations, the reactor core is at a temperature of around 950K. In the case of a power outage, normal operations stop and the decay heat that is produced by the molten salt steadily warms up the reactor core. Within 8 minutes [6] the core reaches the critical temperature of around 1450K at which it melts [5]. Thus, the freeze plug operates appropriately when it melts and drains the molten salt of the reactor vessel within 8 minutes.

1.4 Previous research

In contrast to the recent motivation to develop passive safety systems for nuclear power plants, the concept of the freeze plug has been around significantly longer. As early as in 1960, prototypes of the freeze plug emerged in the research done by ORNL [10]. In the study the freeze plug operated more as a valve, controlling the flow in the early version of the MSR. The use of a so-called freeze valve was desired because a reliable and proven mechanical valve was not available at the time. In contrast to the freeze plug, the freeze valve was melted actively by heating it when necessary. Extensive reports on the design of the freeze valve can be found in [10] and [11].

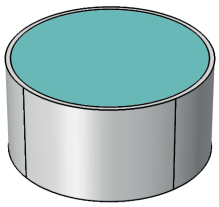

Figure 1.2: Freeze plug design with a single plug [9].

In recent years and with the identified need for a passive draining system, research on the freeze plug was reanimated. First, Swaroop researched the freeze plug by creating a 1-dimensional model [6]. The simple and analytic model resembled a single plug blocking the entire draining pipe, in which heating only occurred at the top of the plug, in the interface between plug and molten salt. The configuration is displayed in figure 1.2. With this configuration Swaroop gathered a melting and draining time of 12 minutes for a plug with a depth of 2 cm [6]. To speed up the melting process van Tuyll [7], and later Makkinje [8], proposed a new design in which multiple freeze plugs are combined in an alloy plug module, as figure 1.3 illustrates. The rationale behind the new configuration, that bears a striking resemblance to a shower drainage, is that the heat transfer to the plugs is increased by the possibility of heat reaching the sides of the plugs through the alloy plug module. It was shown that within the model used the melting time could be reduced to 45 seconds for freeze plugs with a depth of 3 cm [8]. The model, however, did not make use of convective heat transfer and assumed perfect transfer between the molten salt and freeze plug module.

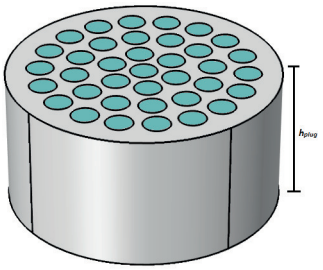

Figure 1.3: Freeze plug design featuring alloy plug module and multiple freeze plugs [9].

A new design was brought forward by Deurvorst [9], in which he introduced cooling fins. The cooling fins were brought in to increase the heat transfer from the alloy plug module to the freeze plugs, in part because the surface area of the alloy module exposed to the molten salt was increased. Also, the model used for the research added in the convective heat transfer from the molten salt flow past the plug module. The report concluded that a configuration of closely staggered fins could decrease melting time. An example of such a configuration is shown in figure 1.4.

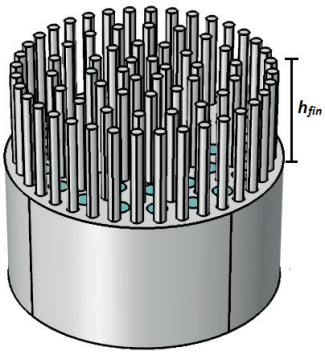

Figure 1.4: Plug design with added cooling fins as proposed by Deurvorst [9].

1.5 Research goals

Since all of the previous research primarily focused on the melting behaviour of the freeze plug in the event of an emergency, the aim of this thesis was directed at the freeze plug during normal operations. More specifically, the present work is dedicated at understanding the cooling requirements for the freeze plug during normal operations of the MSFR. The most principal question this report aims to answer would therefore be:

What are the cooling requirements for a suitable freeze plug module under normal operating conditions?

In this question the suitability of the freeze plug refers to the melting and draining time of previous freeze plug designs being less than 8 minutes. For a large part, the present work is committed on modelling the normal operating conditions of the reactor around the freeze plug in order to accurately retrieve the cooling requirements. The operating conditions are captured by modelling the flow of the molten salt and the heat transfer interaction between the molten salt and the plug. As chapter 2 will further show, the flow above the plug module is in the turbulent regime and thus heat transfer from the flow to the plug is greatly influenced by the velocity profile and laminar sublayer, among other things. The models this thesis features incorporate both flow dynamics and heat transfer. While Deurvorst did include an analytic term for the convective heat transfer, the actual flow was never modelled. In short, the principal research question can be dissected in the following:

(i) What are the effects of the dimension, i.e. the width and height, of the plug on the cooling requirements?

(ii) How does the ratio between freeze plug material and alloy casing influence the cooling requirements?

(iii) How do the turbulent flow characteristics of the molten salt influence the cooling requirements?

1.6 Thesis outline

To answer the questions listed above, the present work is divided in multiple sections. First, the relevant theoretical framework is explained in chapter 2. In this chapter, the MSFR geometry is clarified and theoretical backgrounds for both the molten salt flow and heat transfer modelling are provided. Subsequently, the simulation method used in COMSOL to compute the cooling requirements are elaborated on in chapter 3. This section features a detailed description of the models and a section on the relevant mesh selection. Chapter 4 displays the results of this thesis. In chapter 5 the conclusions, based on the results of the previous chapter, are formulated. Included in this chapter are the recommendations for future research. The report closes out with the bibliography and appendices, in which supplementary graphs, MATLAB scripts and the simulation log are included.

Chapter 2

Theoretical framework

In this chapter the theoretical background of the research is discussed. As stated previously, the research is directed at capturing the normal operating conditions of the MSFR, specifically around the freeze plug. To achieve this, both the flow and heat transfer characteristics of the molten salt and the freeze plug are modelled, since the flow characteristics are closely correlated to the heat transfer of the molten salt to the plug, as will be shown. The chapter starts out with a general section on the molten salt flow in the MSFR, proceeds with providing the theoretical framework of turbulence modelling in COMSOL and concludes with a section on the heat transfer properties of both the molten salt flow and the freeze plug, to understand the heat transfer to the plug from the molten salt flow.

2.1 Molten salt flow in the MSFR

As stated in the previous chapter, an unique feature of Molten Salt Reactors is the fact that the liquid molten salt functions as both a coolant and a fuel. For the MSFR, the molten salt flow consists of a mixture of LiF-ThF_4 (78-22 mol%). Apart from research directly related to the MSFR, not much is known about the physio-chemical properties. Ignatiev [12] studied the properties for specific temperatures around the operating temperatures of the MSFR. The resulting properties are displayed in table 2.1. The third column of the table features the value of the molten salt property at the operating temperature of 950 K.

Table 2.1: Properties of the molten salt LiF-ThF4, the temperature T is in K. The value of C_p for 950 K is extrapolated, since the highest temperature of the validity range is below 950 K. Adopted from [12]

Property	Formula	Value at 950 K	Validity range (K)
ρ ($\mathrm{kg\,m^{-3}}$)	$4.094 \cdot 10^3 - 8.82 \cdot 10^{-4}(T - 1008)$	4124.9	$[893 - 1123]$
ν ($\mathrm{m^2\,s^{-1}}$)	$5.54 \cdot 10^{-8} \cdot \exp(3689/T)$	$2.46 \cdot 10^{-6}$	$[898 - 1119]$
μ ($\mathrm{Pa\,s}$)	ρ ($\mathrm{kg\,m^{-3}}$) $\cdot 5.54 \cdot 10^{-5} \cdot \exp(3689/T)$	$10.1 \cdot 10^{-3}$	$[898 - 1119]$
λ ($\mathrm{W\,m^{-1}\,K^{-1}}$)	$0.928 + 8.397 \cdot 10^{-5} \cdot T$	1.0097	$[891 - 1020]$
C_p ($\mathrm{J\,kg^{-1}\,K^{-1}}$)	$-1111 + 2.78 \cdot T$	1530	$[867 - 907]$

Another relevant property of the LiF-ThF_4 mixture in the present work is the melting temperature. Since the freeze plug cooling requirements are yet to be determined, they could have implications on the temperature of the molten salt flow closely traversing the plug. When the cooling of the plug severely affects the molten salt near the plug, the molten salt could also be cooled to below its melting temperature, possibly causing a layer of solid salt to be formed. E. Cappeli et al. determined the melting temperature of the LiF-ThF_4 mixture used in this thesis to be 848 K [13].

2.1.1 Current design of the MSFR

As the MSFR is still under development, no definitive or realised reactor design is present yet. Since this thesis is part of the SAMOFAR research project, the most current design as proposed by [4] is used. Figure 2.1 provides a clear overview of the most current reactor design. From the geometry it can be gathered that not one but 16 draining pipes will be used in the MSFR, implicating that every freeze plug will have smaller dimensions than in previous designs which featured a single draining pipe. The freeze plugs will be installed at the top of the draining pipe so that no cavity is formed in the draining pipes. The location of the draining pipes and freeze plugs is set in between the pump channel and the core cavity. Furthermore, the size indications provide clear insight into the relevant dimensions for the modelling of the molten salt flow. The specific dimensions used in the experimental models will be further elaborated on in chapter 3.

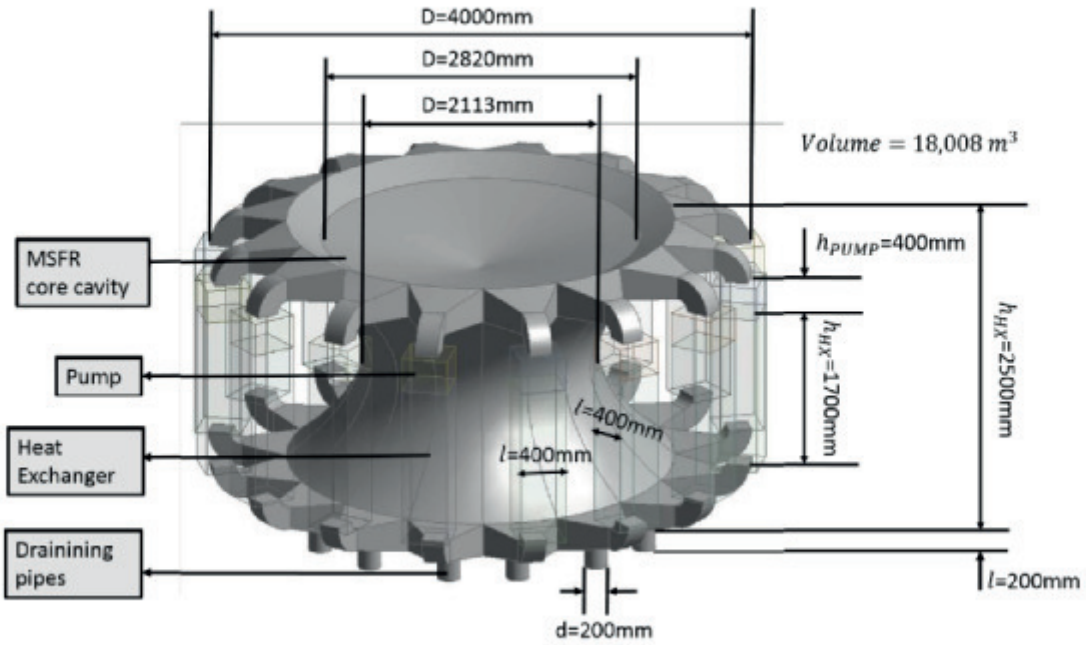

Figure 2.1: Model of the reactor geometry used in this thesis. Adopted from [4].

2.1.2 Flow characteristics in the MSFR

The study provided by [4] on the MSFR fluid dynamics brought forward a velocity distribution of the molten salt flow in the reactor. When considering the freeze plug cooling requirements, the flow near the end of the pump channel is of great interest, since this is where the flow traverses the top of the plug module. This area is explicitly indicated in figure 2.2. The flow velocity distribution, as shown in figure 2.2, states that the flow has an average magnitude of around 3.2 m/s when entering the area of interest. From then on the flow rapidly develops a new velocity profile before passing over the top of the freeze plug. A simplified overview of the geometry around the freeze plug module and draining pipe is presented in figure 2.3. Chapter 3 will shed a light on how the models in this thesis account for the developed velocity profile.

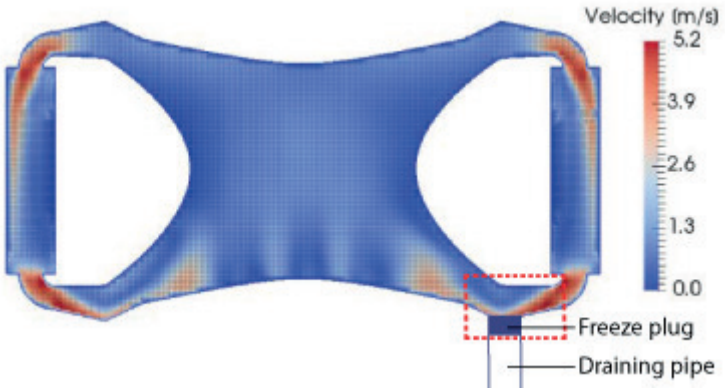

Figure 2.2: Velocity distribution in current reactor design with highlighted area of interest. Adopted from [4]

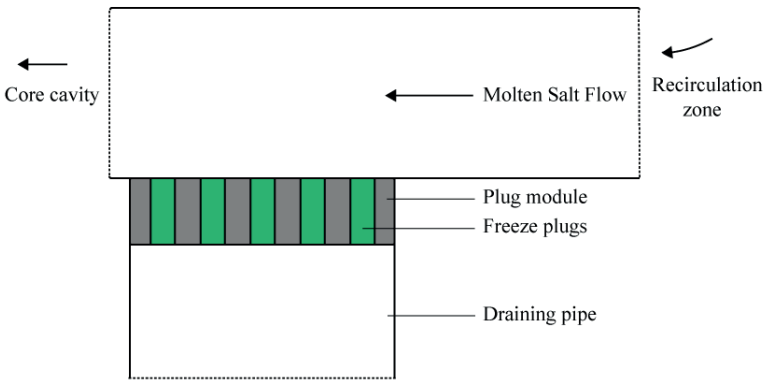

Figure 2.3: Simplified overview of the area of interest, indicated with red frame in figure 2.2

2.2 Turbulence modelling

The molten salt flow is the sole heat source for the freeze plug, as can be seen in figure 2.3. As stated previously do the flow characteristics of the molten salt highly influence its heat transfer to the freeze plug, as will be discussed in detail. In this section, the relevant theory on modelling the molten salt flow is brought forward. The determination of the flow regime is considered first, then the theory on the Reynolds Averaged Navier-Stokes approximation and associated turbulence variables is presented. The section continues with the clarification of the selected COMSOL turbulence models and finishes with some considerations on 2D versus 3D turbulence modelling.

2.2.1 Turbulent flow regime

A conventional way of classifying flows is by their Reynolds number, as given by equation 2.1 [14].

$$Re = \frac{\rho v D}{\mu} \tag{2.1}$$

The Reynolds number is a dimensionless value for the ratio between inertia forces and viscous forces acting on the flow. In equation 2.1, ρ and μ represent the density and dynamic viscosity respectively and are both material properties of the fluid, v is the velocity of the flow and D depicts the characteristic length, which varies per geometry. The Reynolds number of a flow classifies it in one of three main regimes: laminar, transitional or turbulent. The critical Reynolds number, the value for which the flow transitions into the turbulent regime, differs per flow geometry, but through extensive experimentation, critical Reynolds numbers for a myriad of geometries have been determined. The applicable critical Reynolds number for this thesis is the one associated with a channel flow geometry, as chapter 3 will explain further, and its theoretical value is $Re_{crit} = 1800$ [15].
A quick calculation of the Reynolds number for the flow in the area of interest as displayed by figure 2.3 makes use of a characteristic length of 0.15 m (height of the channel), the ρ and μ from table 2.1 and a velocity of 3.2 m/s, as deduced from figure 2.2. When these values are plugged in equation 2.1, a Reynolds number of 196,039 is returned. Since this is clearly larger than Re_{crit}, the molten salt flow is in the highly turbulent regime. This assertion is in agreement with the calculation of the velocity profile in figure 2.2, for which turbulence was also assumed [4].

2.2.2 RANS approximation

In order to successfully model the turbulent flow characteristics in COMSOL, the fundamentals of turbulent flow and its differences with laminar flow must be intimately studied. The primary difference is embedded in the fact that in turbulent flows the velocity ($\vec{u}$) and the pressure (p), in a point, fluctuate in time. The time-dependent fluctuations can be incorporated in the formulation for the flow velocity $\vec{u}$ as follows:

$$\vec{u} = \overline{u} + u' \tag{2.2}$$

In which the time-dependent flow velocity in a point $\vec{u}$ is taken to be the sum of the time-averaged flow velocity $\overline{u}$ and the fluctuations about this mean u' in that point. To account for this distinction, all the turbulence models in COMSOL apply the Reynols Averaged Navier-Stokes (RANS) approximation. Within RANS models, only the time-averaged flow velocity $\overline{u}$ is computed, while the fluctuations u' are accounted for in the form of turbulence variables. The RANS equation COMSOL uses for the mean flow velocity can be written as [16]:

$$\frac{\partial \rho \overline{u_i}}{\partial t} = -\overline{u_i}\frac{\partial \overline{u_i}}{\partial x_i} + \rho g_i - \frac{\partial \overline{P}}{\partial x_i} + \frac{\partial}{\partial x_j}\left[\mu\left(\frac{\partial \overline{u_j}}{\partial x_j} + \frac{\partial \overline{u_j}}{\partial x_i} - \rho\overline{u_i' u_j'}\right)\right] \tag{2.3}$$

From equation 2.3 it can be gathered that the flow is governed by convective flux, represented in the first term on the right hand side, and the summation of the forces acting on the fluid. Gravity forces are not within the scope of the present work and are thus not considered from now on. The summation of forces is therefore formulated as follows:

$$\sum F = -\underbrace{\frac{\partial \overline{P}}{\partial x_i}}_{\text{pressure force}} + \underbrace{\frac{\partial}{\partial x_j}\left[\mu\left(\frac{\partial \overline{u_j}}{\partial x_j} + \frac{\partial \overline{u_j}}{\partial x_i} - \rho\overline{u_i' u_j'}\right)\right]}_{\text{shear stress}} \tag{2.4}$$

The quantities of all the terms can be calculated by using the mean flow velocity $\overline{u}$, except for the last term of the shear stress, which includes the fluctuations about the mean flow u_i' and u_j'. The term $-\rho\overline{u_i' u_j'}$ is known as the Reynolds shear stress and in order to solve for the mean flow, it should be formulated in terms of known quantities. As a first step to achieving this, all turbulence models in COMSOL make use of the Bousinessq approximation [15], which allows the Reynolds shear stress τ_{ij} for an incompressible fluid ($\nabla.\overline{u} = 0$) to be formulated as [16]:

$$\tau_{ij} = -\rho\overline{u_i' u_j'} = \mu_T\left[\frac{\partial \overline{u_i}}{\partial x_j} + \frac{\partial \overline{u_j}}{\partial x_i}\right] \tag{2.5}$$

Due to the approximation, the Reynolds shear stress is expressed as a function of the known gradients of the mean flow through the construction of μ_T, the turbulent viscosity. The turbulence models in COMSOL all have a distinct way of calculating μ_T, which is one of the two differentiating categories. The second differentiating factor is the way a turbulence model treats the flow near a wall. The models in COMSOL offer two wall treatment configurations, namely no slip and wall functions, which will both be addressed in length somewhat further in this chapter. An overview of some of the frequently used turbulence models in COMSOL is provided in table 2.2.

Table 2.2: Frequently used COMSOL turbulence models [17].

Turbulence Model	Turbulent Viscosity	Wall Treatment
Algebraic yPlus	$\mu_T = \rho l_{mix}^2 \frac{\partial U}{\partial y}$	No slip
k-ω (SST)	$\mu_T = \frac{\rho a_1 k}{max(a_1\omega, S f_{v2})}$	No slip
k-ϵ	$\mu_T = \rho C_\mu \frac{k^2}{\epsilon}$	Wall functions
k-ω	$\mu_T = \rho C_\mu \frac{k}{\omega}$	Wall functions

The most widely used model would be k-ϵ, since models featuring wall functions take drastically shorter computation time and give fairly accurate results for the mean flow solution. Models employing the no slip condition in general take longer computation times. Their accuracy for evaluating the flow near the wall, however, is certainly superior when compared to models using wall functions. In this thesis, both the k-ϵ and the Algebraic Yplus model were used to compute the molten salt flow.

2.2.3 k-ϵ turbulence model

From table 2.2 it can be gathered that the k-ϵ turbulence model is distinct in its mathematical relation for μ_T and its wall treatment procedure. From table 2.2 it can be deduced that:

$$\mu_T = \rho C_\mu \frac{k^2}{\epsilon} \tag{2.6}$$

In which ρ is the density of the fluid and C_μ a constant that is experimentally determined to bo equal to 0.09. In the model, k and ϵ make up the turbulence variables, in which k is the turbulent kinetic energy (TKE) and ϵ the turbulent dissipation. The model incorporates two extra transport equations, for k and ϵ, to account for the turbulent properties of the flow and is hence called a two-equation turbulence model. First, k and the associated transport equation are discussed. Pope [16] formulates the TKE k in terms of flow velocity fluctuations in a point:

$$k = \frac{1}{2}\left(\overline{(u_i')^2} + \overline{(u_j')^2} + \overline{(u_k')^2}\right) \tag{2.7}$$

In which the subscripts i,j,k depict the 3 dimensions in which the fluctuations may arise. The associated transport equation for k can be specified as [16]:

$$\frac{\partial(\rho k)}{\partial t} + \frac{\partial(\rho k u_i)}{\partial x_i} = \frac{\partial}{\partial x_j}\left[(\mu + \mu_T/\sigma_k)\frac{\partial k}{\partial x_j}\right] + P_k - \rho\epsilon \tag{2.8}$$

Through equation 2.8 it can be gathered that the rate of change of k is made up of transport of k by convection (first term on right hand side), diffusive transport of k (second term), a production term P_k and a term for the dissipation of k, namely $\rho\epsilon$. In the diffusive term, the σ_k is a empirically determined constant with a value of 1. For the production term P_k the following applies:

$$P_k = \tau_{ij}\frac{\partial U_i}{\partial x_j} \tag{2.9}$$

In equation 2.9, τ_{ij} represents the Reynolds shear stress as defined in equation 2.5 and U_i depicts the free flow velocity. From the equation it can be gathered that turbulence is generated from the free velocity flow in the direction perpendicular to the mean flow velocity. Also, from equation 2.8, it is deduced that ϵ is the dissipation rate of k. More specifically, ϵ is a measure for the rate at which turbulent kinetic energy k is converted into thermal internal energy. Similar formulas are formulated for ϵ [16].

$$\epsilon = \nu\overline{\frac{\partial u_i'}{\partial x_k}\frac{\partial u_i'}{\partial x_k}} = \frac{C_\mu^{3/4}k^{3/2}}{l} \tag{2.10}$$

$$\frac{\partial(\rho\epsilon)}{\partial t} + \frac{\partial(\rho\epsilon u_i)}{\partial x_i} = \frac{\partial}{\partial x_j}\left[(\mu + \mu_T/\sigma_\epsilon)\frac{\partial \epsilon}{\partial x_j}\right] + C_{\epsilon 1}\frac{\epsilon}{k}P_k - C_{\epsilon 2}\rho\frac{\epsilon^2}{k} \tag{2.11}$$

In equation 2.10, l is a measure for the turbulence length. The introduced constants in equation 2.11 all have an empirical base and are determined to be $\sigma_\epsilon = 1.3$, $C_{\epsilon 1} = 1.44$ and $C_{\epsilon 2} = 1.92$. From both transport equations it is concluded that turbulent kinetic energy k is produced mainly from the larger scale free flow velocity and then dissipated at a rate ϵ into thermal internal energy.

Since COMSOL performs an iterative computation of the equations listed above, educated estimates for the initial values of k and ϵ need to be done. In his work, Zijlema [18] proposed several ways of defining initial values of k and ϵ for different geometries. For a channel flow, the following relations for k and ϵ hold.

$$I_T = \frac{\sqrt{2/3k_{in}}}{u} \tag{2.12}$$

Here, I_T is the turbulent intensity. Throughout literature, it is often taken to be 1%. For the initial value of the velocity we make the assumption that the streamwise velocity is uniform and is equal to the free flow velocity of the bulk U_B. For ϵ the assumption is made that l_{mix} equals $0.03H$, where H is the height of the channel. Hence by rewriting equation 2.12 and by using equation 2.10 we can deduce that the inlet profiles are [18]:

$$u_{in} = U_B, \quad k_{in} = 1,5 * 10^{-4} u_{in}^2, \quad \epsilon_{in} = \frac{C_\mu^{3/4} k_{in}^{3/2}}{0.03H} \tag{2.13}$$

From table 2.2 it becomes apparent that the $k-\epsilon$ model in COMSOL makes use of wall functions for its computation of the flow near the wall. This means that instead of explicitly evaluating the flow near the wall, it uses an analytical expression to evaluate the turbulence variables k,ϵ and μ_T near the wall. The reason for employing wall functions is twofold. First off, explicitly computing the flow near the wall requires a highly refined mesh and thus takes significantly longer computing times. Secondly, in the region very close to the wall, the turbulence relations as put forth by equations 2.7 to 2.11 don't hold anymore, since the fluid velocity at the walls is zero. This implies that both the mean flow velocity $\overline{u}$ as well as the fluctuations u' are equal to zero, and from equations 2.6 to 2.7 it becomes clear that the turbulent variables k and μ_T are also equal to zero. To still being able to solve for the flow near the wall, the model makes use of the law of the wall [17].

Law of the wall

The law of the wall postulates that for many different flow conditions, the velocity profile of the flow in the region very close to the wall has the same shape. In order to compare flows more efficiently, some dimensionless variables are introduced for describing the velocity profile in the boundary layer.

$$u^+ = \frac{u}{u_\tau}, \quad y^+ = \frac{y u_\tau}{\nu}, \quad \nu_T^+ = \frac{\nu_T}{\nu} \tag{2.14}$$

Within these formulations, ν represents the kinematic viscosity and the subscript T denotes turbulence. The variable y is the perpendicular distance from the wall and u_T represents the shear velocity, used to scale the flow velocity. It is specified by the shear stress balance near the wall:

$$(\mu + \mu_T)\frac{\partial U}{\partial y} = \tau_{wall} = \mu \frac{\partial u}{\partial y} = \rho u_\tau^2 \tag{2.15}$$

The above relation establishes that the wall shear stress τ_{wall} is equal to the turbulent and viscous shear stress. Using the dimensionless variables u^+, y^+ and ν_T^+, a velocity profile in the boundary layer is constructed in figure 2.4 that applies to a wide range of flows. Three distinct regions are identified in the boundary layer of the flow. Closest to the wall is the laminar sublayer, named after the fact that only viscous forces act on the flow. Then comes the buffer layer, in which the first turbulent structures manifest itself. Lastly in the boundary layer we identify the log-law region, in which, as will be shown, the velocity profile is described using a logarithmic relation.

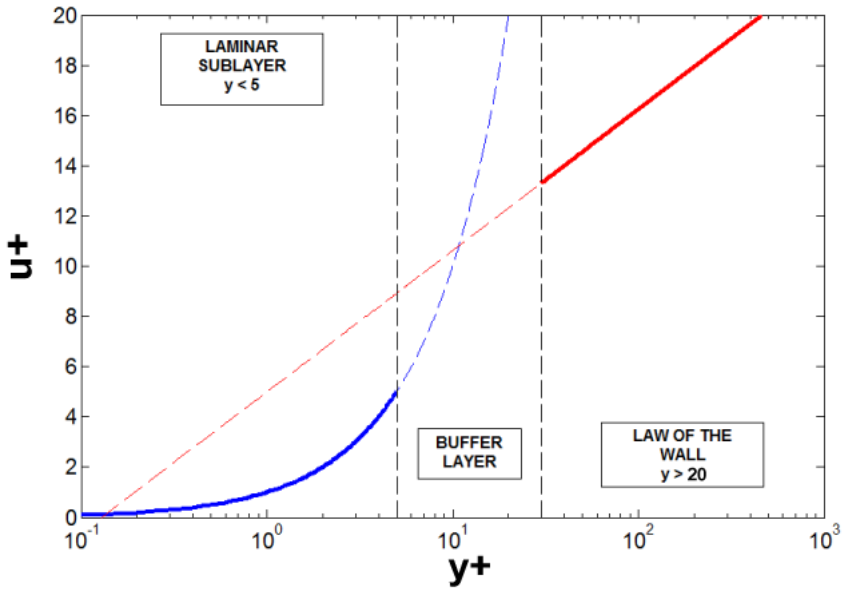

Figure 2.4: Velocity profile of a turbulent flow near the wall in dimensionless coordinates. Adopted from [19].

The velocity profile is displayed using the normalised velocity u^+ and a logarithmic scale of y^+. For the different regions, relations can be formed for the velocity profile in terms of the dimensionless variables. These relations are shown below, their derivations can be found in [16].

For the laminar sublayer ($0 < y^+ < 5$) is holds that:

$$u^+ = y^+ \tag{2.16}$$

In figure 2.4 the profile in the laminar sublayer takes on a parabolic shape, but since it is plotted on a logarithmic y^+ axis, the relation is in fact linear.

For the buffer layer ($5 < y^+ < 20$) no explicit velocity profile is determined. It acts solely as a transitional layer from the laminar layer, dominated by viscous forces, to the log-law layer, in which turbulence starts playing its part.

For the log-law layer ($y^+ > 20$) the law of the wall holds true for the velocity profile. This is, as expected, a logarithmic relation.

$$u^+ = \frac{1}{\kappa} \ln(y^+) + B \tag{2.17}$$

Where κ is the von Karman's constant and is equal to 0.41 and the constant B holds a value of 5.1. It is equation 2.17 that the $k-\epsilon$ model in COMSOL uses to model the flow near the wall. Since the law for the wall holds for a wide variety of flows, the model virtually places its first computational node in the log-law region in the limit $y \to 0$ irrespective of the total mesh refinement. Figure 2.5 gives insight in how the first computational node is placed with respect to the wall.

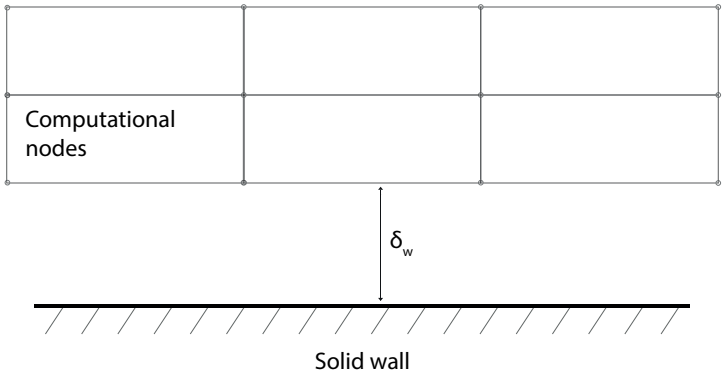

Figure 2.5: Schematic representation of the first computational node selection with wall functions.

From figure 2.5 it can be gathered that the virtual displacement δ_w is the perpendicular distance form the first computational node of the mesh to the wall. The model calculates δ_w by assuming a value of y^+=20 and subsequently solving for equations 2.14. By doing this, the model is able to generate a converging result for the mean flow relatively quickly, because the viscous sublayer with high velocity gradients is not solved for while at the same time retaining accuracy in the mean velocity profile because equations 2.7 to 2.11 do not hold in the viscous sublayer.

2.2.4 Algebraic yPlus model

From table 2.2 can be deduced that one of the principal differences with the $k-\epsilon$ model is that it does not employ wall functions. Instead, it computes the mean flow from the viscous layer and upwards. For this, the mesh resolution near the wall will have to be much finer compared to the $k-\epsilon$ model. For accurate results, a minimum of three computational nodes [16] should be present in the viscous layer, with the outer most node within a distance of $y^+ = 1$.
As stated before, the turbulent flow behaviour of the molten salt has a major impact on its heat transfer to the freeze plug. When using the wall functions as described above, the virtual displacement δ_w of the first computational node with respect to the wall could act as an insulating layer of sorts, interfering with correctly modelling of the heat transfer between the molten salt flow and the freeze plug. The conductive heat transfer could specifically suffer a severe impact from this. Because the Algebraic yPlus model models the flow directly from the wall and up, it was also employed in this thesis.
In table 2.2, the relation for the turbulent viscosity μ_T the yPlus model uses is displayed. The dynamic viscosity is for the Algebraic yPlus model is given by:

$$\mu_T = \rho l_{mix}^2 \frac{\partial U}{\partial y} \tag{2.18}$$

Because the Algebraic yPlus model constructs the mean flow solution from the wall up, it is convenient to rewrite the above equation using the dimensionless variables of equation 2.14. This yields [6]:

$$\left(1 + l_{mix}^2 \frac{\partial u^+}{\partial y^+}\right) \frac{\partial u^+}{\partial y^+} = 1 \tag{2.19}$$

Where l_{mix} is the mixing length, a measure for the length the flow can retain its lateral velocity for which the model uses the definition based on the Prandtl mixing length theory. The theory asserts that the mixing length is zero in the viscous sublayer because viscous forces dominate the flow dynamic there. Far away from the wall, l_{mix} scales with y^+:

$$l_{mix} = \begin{cases} 0 & y^+ < y^* \\ k \cdot y^+ & y^+ \geq y^* \end{cases} \tag{2.20}$$

Where y^* denotes the distance form the wall at which the mixing length starts getting a value, i.e. the distance where turbulent phenomena start occurring and κ the von Karman's constant as used in equation 2.17. Incorporating equation 2.20 in equation 2.19 and integrating for u^+ returns the following:

$$u^+ = \begin{cases} y^+ & y^+ < y^* \\ y^* + \frac{1-\sqrt{1+4\kappa^2(y^+-y^*)^2)}}{2\kappa^2(y^+-y^*)} + & \\ \frac{1}{\kappa}\left(\ln\left(\left(\sqrt{1+4\kappa^2(y^+-y^*)^2)}\right)\right) + 2\kappa(y^+-y^*)\right) & y^+ \geq y^* \end{cases} \tag{2.21}$$

If y^+ is sufficiently large, i.e. $y^+ >> y^*$, the above formula reduces to [6]:

$$u^+ = y^* + \frac{1}{\kappa}\log\left(y^+\right) + \frac{1}{\kappa}(\log(4\kappa) - 1) \tag{2.22}$$

For large values of y^+ the velocity profile u^+ should take on the form as prescribed by the law of the wall, as stated in equation 2.17. Therefore, it can be deduced that y^* is equal to:

$$y^* = B - \frac{1}{\kappa}(\ln|4 \cdot \kappa| - 1) \tag{2.23}$$

With B being the same constant as used in equation 2.17 with a value of 5.1. In order to complete the computation for u^+, l_{mix} and μ_T and to subsequently compute the mean flow velocity, it is required to define y^+. This is done using the local Reynolds number, which can be formulated as:

$$Re = \frac{uy}{\nu} = \frac{u}{u_\tau} \cdot \frac{u_\tau y}{\nu} = u^+ y^+ \tag{2.24}$$

The variables in the first expression of the local Reynolds number (u, y and ν) are solved for on each node and then y^+ is calculated by using the expression for u^+ given in equation 2.21.

2.2.5 2D approximation

Intrinsically, turbulence is a 3-dimensional phenomenon. In this thesis, the simulations of the molten salt flow are all 2-dimensional. The main drivers for this approximation are listed below.

1. The foremost reason that a 2D approximation was preferred for this thesis is that the fully developed mean channel flow of the molten salt is symmetrical around the y-plane. In this regard, a 2D representation of the mean flow provides the same accuracy as computing the 3D mean flow.

2. The increase in mesh elements needed for 3D models bring about far longer computation times when compared to 2D models. The difference is so significant, differing from a computation time of around 20 hours for 3D to 20 minutes for 2D on average, that it was a relevant driver in the choice for the 2D approximation.

3. The velocity profile within the reactor as shown in figure 2.2, is only known in 2D. Since it functions as a starting point for the simulations in the present work, the 2D geometries in this thesis were in agreement with this.

4. The most notable disadvantage of the 2D approximation is that the freeze plug itself is not symmetrical around the y-plane, because of its circular geometry. This could influence the cooling requirements, since the flow, in the current models, traverses the plug surface over the full distance of its diameter. In reality though, the flow also traverses the plug over a smaller distance more to the side of the circular surface. The discrepancy between the 2D approximation of the plug geometry should be considered in the interpretation of the results of the models.

2.3 Heat transfer

In the simulation models, two distinct domains can be identified. First the domain of the molten salt flow is recognised, and secondly the plug module domain, consisting of the alloy plug module and the freeze plugs, is established. This section will lay bare the applicable theoretic framework concerning heat transfer in each domain.

In general, three types of heat transfer are identified, namely convective and conductive heat transfer and heat transfer through radiation. The latter is not considered within the present work, mainly due to the fact that the effects of radiation in the freeze plug and molten salt interaction are negligible. In effect, two main ways of heat transfer are considered: conductive and convective heat transfer. In the plug module domain, solely conductive heat transfer plays a role, since the entirety of the module is in its solid state. The molten salt flow domain does feature both conductive and convective heat transfer.

2.3.1 Heat transfer in plug domain

In the plug module domain, only conductive heat transfer occurs. The plug module does present a complication in its configuration of both alloy plug casing and freeze plug material that poses an influence on the conductive heat transfer.
Conductive heat transfer occurs when molecules transfer a net amount of heat without transporting any mass. The heat of molecules with higher internal energy is transferred to molecules with a lower internal energy through microscopic collisions. In this way the heat is distributed spontaneously within a body, until a thermal equilibrium is reached. It is therefore no surprise that the governing equation for heat conduction, Fouriers law, features the temperature gradient ∇T [14]:

$$\vec{q}^{"}_{cd} = -\lambda \nabla T \tag{2.25}$$

In Fouriers law, a temperature gradient in a particular direction drives a conductive heat flux $\vec{q}^{"}_{cd}$ in the opposing direction, essentially implying that heat is always conducted from hot to cold areas. The heat flux scales with the thermal conductivity λ as specified in table 2.1. The thermal conductivity is therefore a measure for how easily heat is conducted within a material.
Fouriers law is the governing equation for heat conduction in a single solid body, but needs to be expanded on when conduction takes place over multiple solid bodies. In the present work, multiple interfaces between solid bodies are identified between the alloy casing and the freeze plugs, as was shown in figure 1.3.

A popular way of envisioning conduction through multiple solid bodies is the thermal resistance analogy. It states that, analogous to Ohms law for electrical resistance, the total conductive thermal resistance in 1 dimension is expressed by dividing the driving heat force ΔT by the flux of conductive heat q''_{cd} [14]:

$$R_{tot,cd} = \frac{\Delta T}{q''_{cd}} \tag{2.26}$$

When considering the interface between the alloy casing and the freeze plug, the total conductive resistance takes on the following form:

$$R_{tot,cd} = \frac{D_{Alloy}}{\lambda_{Alloy}} + R_{contact} + \frac{D_{Plug}}{\lambda_{Plug}} \tag{2.27}$$

In which λ stands for the thermal conductivity of the appropriate material and D symbolizes the distance through which the heat is conducted.

2.3.2 Heat transfer in molten salt domain

Whereas the heat transfer in the plug domain is captured with relative ease by solely considering conductive heat transfer, the molten salt domain proposes a much more complicated situation. In part because the medium in the domain, the LiF-ThF_4, is a liquid and thus convective heat transfer also plays its part, but mainly because the molten salt flow is in the turbulent regime. For turbulent flows, as is the case for the flow velocity $\vec{u}$, the temperature T at a point in the domain experiences small time-dependent perturbations around the time averaged mean temperature $\overline{T}$:

$$T = \overline{T} + T' \tag{2.28}$$

Similarly to the RANS approximation and the need to model the Reynolds stress for the mean flow velocity transport equation, the time-dependent perturbations in the temperature at each point in the domain also require to solve for the turbulent heat fluxes associated with them. It is, however, not within the scope of the present work to model the heat transfer within the entire molten salt domain. The turbulent heat transfer dynamics in the bulk of the flow velocity do not make up a topic of research, whereas the heat transfer from the molten salt flow through the plug channel interface does very much so. This allows for a more focused approach in providing the relevant theoretic background on the heat transfer in the molten salt domain. More specifically, the situation of a turbulent channel flow passing over a surface that is cooled allows to capture the heat transfer between plug and molten salt flow by using an analogy between mass, momentum and heat transfer, specifically conductive heat transfer.
Convection arises when heat is transferred through the transportation of mass. Usually the mass is transported through the movement of fluids. Within the broader term, forced and natural convection are distinguished. Natural convection only arises when gravitational forces are in play and the local differences in density are the driver of movement. Since gravitational forces are not considered, only forced convection is discussed in this thesis. In this thesis, the convective heat transfer occurs between the molten salt flow and the surface of the freeze plug.
The leading equation in convective heat transfer would be Newtons law of cooling, which describes the heat flux due to convection from a surface to the surrounding medium in the following way.

$$q''_{cv} = k(T_{surr} - T_s) \tag{2.29}$$

In the above equation, k is the heat transfer coefficient. T_{surr} is the temperature of the surrounding medium and T_s is the temperature of the surface. The heat transfer coefficient is a measure of how easily heat is transferred from the surface of a solid body to its surroundings. The value of k is dependent on a variety of variables, such as the involved materials and the flow configurations of the surrounding medium. The heat transfer coefficient k can be made dimensionless by introducing the Nusselt number through the following relation, in which D is the characteristic length scale, as defined in equation 2.1, and λ is the thermal conductivity, as used in equation 2.25 [14].

$$Nu = \frac{kD}{\lambda} \tag{2.30}$$

As stated above, the heat transfer coefficient, and subsequently the Nusselt number, vary for different configurations of the surface and the surrounding medium. Finding the right Nusselt relation for the configuration at hand is essential in determining the right convective heat transfer. For determining the Nusselt relation for the molten salt flow and the surface of the freeze plug, the Chilton-Colburn analogy is considered.

Chilton-Colburn analogy

The Chilton-Colburn analogy is a widely used relation between heat, momentum and mass transfer. The analogy is especially suitable for highly turbulent flows with a $Re > 10,000$, which is the case in this thesis. First, the analogy itself is provided, before some of its parts are expanded on [20].

$$\frac{Nu}{RePr^{1/3}} = \frac{c_f}{2} \tag{2.31}$$

The relation contains both the Reynolds and Nusselt number, as described in equations 2.1 and 2.30 respectively. From equation 2.1 it was gathered that the Reynolds number for the molten salt flow has a value of 196,039. It also includes the dimensionless Prandtl number Pr, and the skin-friction coefficient c_f. The Prandtl number holds a value that is material specific and is given by [14]:

$$Pr = \frac{\nu}{\alpha} = \frac{\mu/\rho}{\lambda/(C_p\rho)} = \frac{\mu C_p}{\lambda} \tag{2.32}$$

The Prandtl number expresses the ratio between the momentum and heat diffusivity by dividing the kinematic viscosity ν by the thermal diffusivity α, which can be simplified to dividing the product of the dynamic viscosity μ and the specific heat C_p by the thermal conductivity λ, which are all intrinsic properties of the material. For the molten salt, LiF-ThF_4, the Prandtl number at the operating temperature of 950K can be calculated by using the properties found in table 2.1. This results in a Prandtl number of Pr=15.95.

The skin-friction coefficient c_f is given by the following relation, that includes the wall shear stress τ_{wall} and the free flow velocity U_0:

$$\frac{c_f}{2} = \frac{\tau_{wall}}{\rho U_0^2} \tag{2.33}$$

Pope [15] deduced that, by using the velocity profile of the log law layer as proposed by equation 2.14, this can be rewritten as:

$$\sqrt{\frac{2}{c_f}} = \frac{1}{\kappa}\ln\left(Re_\delta\sqrt{\frac{c_f}{2}}\right) + 7.2 \tag{2.34}$$

Of which the derivation can be found in Appendix A. Equation 2.34 describes the skin-friction coefficient c_f implicitly and features the boundary layer Reynolds number Re_δ, which is given by equation 2.35.

$$Re_\delta = \frac{U_0 \delta}{\mu} \tag{2.35}$$

In which δ symbolizes the height of the boundary layer. In a fully developed channel flow, as is the case for the molten salt flow, the height of the boundary layer is simply half of the height of the channel, so the value of Re_δ is essentially $0.5 \cdot Re$. Due to the implicit nature of equation 2.34, it is required to solve for c_f iteratively and then produce a fit for the relation with Re_δ. The iterations and plot of the fit are stored in Appendix A, and bring forward the following relation:

$$c_f = 0.0205 Re_\delta^{-1/6} \tag{2.36}$$

Using the relations given in equations 2.32 to 2.36, the Chilton-Colburn analogy takes on the following form in describing the Nusselt number and can be computed when using Re=196039, $Pr = 15.95$ and $c_f = 2.97 \cdot 10^{-3}$ by the following.

$$Nu = RePr^{1/3} \frac{c_f}{2} \tag{2.37}$$

Which yields a value of $Nu = 726.1$ for the geometry at hand. As such, the heat transfer coefficient k can be deduced and the convective heat transfer from the surface of the freeze plug can be evaluated using equation 2.29. It should be noted that for the characteristic length D in equation 2.30 the height of the boundary layer should be used. As noted, for a fully developed flow, the boundary layer is taken to be half of the total channel height, resulting in a value for D of 0.075 m. The value of heat transfer coefficient k /therefore comes down to 9681,3 W/m^{2}K.

Chapter 3

Numerical simulation

After the familiarisation of the relevant theoretical framework, the actual experimental simulations are to be performed. In the present work, all simulations are done through COMSOL Multiphysics [17]. In this chapter, all COMSOL simulation models are explained in stages. First off, the geometries of the different models and the relevant materials are discussed as part of the section on the experimental set up. Secondly, the simulation method is paid attention to. In this section, the relevant COMSOL physics modules, initial values and boundary conditions that play a role are examined. Also, the computation and post processing phase are highlighted in this section, in which the mesh selection in COMSOL and the processing of the retrieved data in MATLAB [21] are included. Lastly, the different models are explicitly presented.

3.1 The experimental set up

As section 1.6 identified, the principal aim of this thesis is to uncover the appropriate cooling requirements for the freeze plug during normal reactor operations. In particular, the area around the freeze plug is of interest. In figure 2.3, a simplified overview is given of the area in the reactor surrounding the freeze plug module. When considering the cooling requirements, the following geometry parameters, as defined in figure 3.1, pose an influence.

- $L_{channel}$ length of the channel
- L_{back} length of the channel section after the freeze plug
- $H_{channel}$ height of the channel
- H_{plug} height of the plug module
- D_{module} diameter of the freeze plug module, equal to $2 \cdot R_{module}$
- D_{plug} diameter of a single freeze plug, equal to $2 \cdot R_{plug}$
- F_{plug} distance between adjacent freeze plugs
- A_{alloy} area of the alloy casing

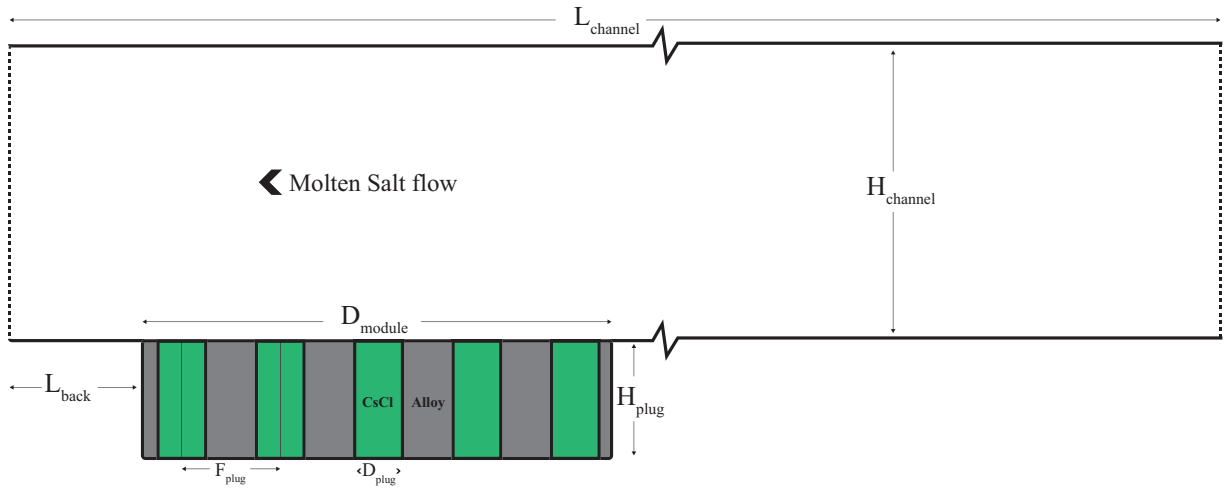

Figure 3.1: Parametrization of the model geometry as used in this thesis [22].

The geometry provided in figure 3.1 is a simplification of the actual area surrounding the freeze plug in the reactor. The simplification mainly lies in the straightening of the walls on the side of the molten salt flow and the 2D approximation of the real situation. As the 2D approximation was already considered in chapter 2.2.5, only the geometrical simplification regarding the walls of the channel are considered here.
When comparing figure 3.1 to the reactor design in figure 2.2, it can be seen that the lower wall is in fact at a slightly downward slope. In the geometries in this thesis, the slope of both walls is taken to be zero, effectively creating a channel flow. Two main reasons exist for the simplification, The first being that the primary aim of this thesis is to understand the fundamental interplay of the molten salt flow and heat transfer. Adding a deviating geometry unnecessarily complicates the interaction and is thus distracting from the key issue. Having understood the fundamentals of the interaction, should the influence of the preceding geometry in the reactor be investigated further. The second reason is that by taking both planes to be parallel an authentic channel flow is effectively created. Within fluid dynamics, channel flow is defined as the flow between two infinite and parallel plates. By doing so, there are a lot of supporting studies and experimental results available, which can act as a reference to validate the research in this thesis.

The cooling of the plug is modelled as a volumetric heat sink, $P_{cooling}$, which has the unit of [W/m^3]. The cooling power $P_{cooling}$ is assigned homogeneously to the alloy parts of the geometry. The reason for this stems from the fact that a cooling system will probably be set up in or around the alloy plug module, since incorporating it into the freeze plugs themselves would inhibit their ability to let the molten salt through in case of an emergency. The assertion that the cooling is distributed homogeneously is more intimately discussed in chapter 5.
In the research, multiple models were used to investigate the cooling requirements for the freeze plug, whose geometries all stem for the one presented in figure 3.1. Various models, however, differ in some ways regarding their geometry. First, the standard values for the geometry are presented and motivated for, and in section 3.3 the ways in which the different models differ from this are discussed separately. For the length of the channel, as will be explained further on, the assertion was made that the flow was fully developed when entering the channel. The lion's share of the parameters were initially based on the research by Deurvorst [9], and are varied later on.

Table 3.1: Standard dimensions of the model geometry as presented in figure 3.1. N_{plugs} represents the number of plugs.

Parameter name	Value and unit	Explanation
$L_{channel}$	1.00 m	Flow is already developed
L_{back}	0.15 m	To determine if flow past plug is affected
$H_{channel}$	0.15 m	Based on reactor design as in figure 2.1
H_{plug}	0.08 m	Based on previous research [9]
D_{module}	0.40 m	Based on previous research [9]
D_{plug}	0.04 m	Based on previous research [9]
F_{plug}	0.08 m	Based on previous research [9]
A_{alloy}	0.016 m^2	In 2D: $A_{alloy} = D_{module} \cdot H_{plug} - N_{plugs} \cdot D_{plug} H_{plug}$

3.2 The simulation method

As described in the beginning of this chapter, defining the geometry of a model is but one of several steps in the general work flow of COMSOL. A subsequent step is the choice of materials for the model. After assembling the geometry and specifying the materials, the applicable physics modules need to be appointed and the appropriate boundary conditions and initial values need to be established. In order to run the model, a mesh must be selected and after computing the model the results are post-processed. These steps dictate the work flow in COMSOL and are used as the structure for this section.

3.2.1 Material selection

In COMSOL, materials are easily implemented in a model by the built-in materials library. Through it, materials and their properties can be assigned to individual parts of the model geometry. For the models in this thesis, as portrayed in figure 3.1, three different materials are used. For the molten salt flow, liquid Lithium Fluoride, LiF, is selected from the materials library, but its properties are updated to match those displayed in table 2.1. The alloy plug module and the freeze plugs themselves remain. Based on the findings in [8], Caesium Chloride, CsCl, is selected for the freeze plug material and Hastelloy N is the alloy of choice for the plug module. Table 3.2 features some of the relevant properties of the solid materials at T = 800 K and some of the LiF-ThF_4 at T = 950 K, with the assumption that these will roughly be the eventual operating temperatures.

Table 3.2: Some of the thermal and physical properties the materials used in the COMSOL models.

Material	λ $[\frac{W}{m \cdot K}]$	C_p $[J\frac{}{kg \cdot K}]$	ρ $[\frac{kg}{m^3}]$	T_{melt} [K]
CsCl	1.3	365	3650	918
Hastelloy N	22.5	580	8620	1645
LiF-ThF_4	1.01	1530	4125	848

3.2.2 Physics modules

The present problem is embedded in a duality of relevant physics: heat transfer and fluid dynamics. As was shown previously, the flow is in the turbulent regime, and both the $k-\epsilon$ and the Algebraic yPlus module are used to model it. In COMSOL, one of both can be selected and configured per model separately. Because the Algebraic yPlus module does not feature wall functions of itself, a separate study node for the wall distance calculation is required. During the wall distance calculation, the appropriate values for y^+ are calculated for the used geometry. Regarding the heat transfer, both the heat transfer module and the non-isothermal flow module are needed to correctly account for the change in temperature in the molten salt flow.

3.2.3 Boundary conditions and Initial values

Within most of the physics modules, there exists a need to establish boundary conditions and initial values in order to perform a successful simulation. An accurate determination of and motivation for the appropriate boundary conditions and initial values are paramount for the success of a model, since they purport a most significant impact on its results. Since both the heat transfer and the turbulent flow module require separate boundary conditions and initial values, they are discussed individually.

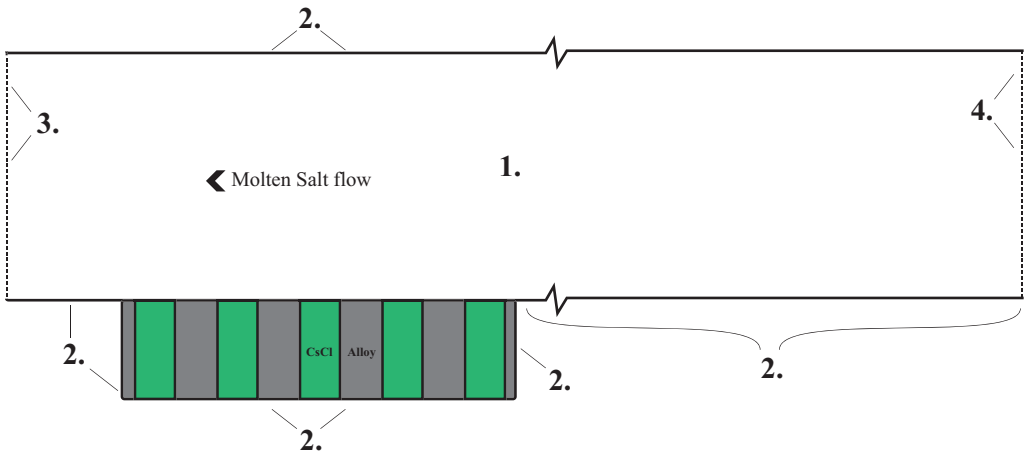

Figure 3.2: Overview of the various boundaries and domains for the heat transfer module.

Figure 3.2 allocates the various boundaries and domains within the geometry. Below a list is presented with a lineup of the boundary conditions and initial values for the heat transfer module, as marked by their number:

1. Initial value - This initial value concerns the entire domain, including the entire freeze plug module and the molten salt flow. In COMSOL, an initial temperature should be specified and in this thesis it is taken to be the normal operating temperature, equalling 950 K.

2. Boundary condition - For most of the boundaries of the geometry, the insulation boundary condition applies. Both the top and bottom wall, excluding the plug and flow interface, are configured to be insulated, meaning no heat will pass through them. The condition also applies to the sides and bottom of the plug module. The draining pipe, the boundaries of the plug, is assumed to behave the same as the walls of the channel.

3. Boundary condition - This boundary is defined as the outflow for the heat transfer. The mathematical formulation is as follows: $-\vec{n} \cdot \vec{q} = 0$, meaning that the heat flow $\vec{q}$ normal to the outflow boundary is zero. The heat flow is proportional to the temperature derivative ∇T according to equation 2.25, and thus the temperature derivative normal to the outflow boundary is also zero in the outflow boundary.

4. Boundary condition - This boundary acts as the inflow of heat by the incoming flow. The heat transfer boundary condition is established by posing a constant temperature of T_{in}= 950 K on the boundary.

To complete the boundary conditions and initial values, those relevant for the turbulent molten salt flow should be discussed. Figure 3.3 appoints the relevant boundaries and domains.

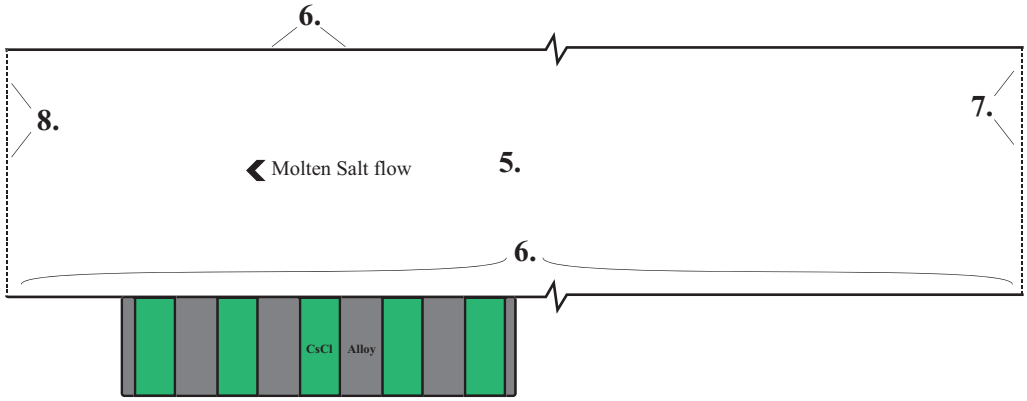

Figure 3.3: Overview of the turbulent flow boundaries and domains.

Since the turbulent flow modules only apply to the channel domain, no boundary conditions or initial values need to be established for the plug module. Some of the boundary conditions and initial values differ between the $k-\epsilon$ and the Algebraic yPlus modules. The following is, again, a listing of the boundary conditions and initial values as specified in figure 3.3:

5. Initial value - For both the $k-\epsilon$ and the Algebraic yPlus module the initial values for the channel domain consist of the temperature T, the density ρ and the dynamic viscosity μ. The temperature T its input is specified as the output of the heat transfer module, and for the density ρ and the dynamic viscosity μ a reference is made to the property values as specified in table 2.1.

6. Boundary condition - For the upper and lower wall the conditions differ per module used. For the $k-\epsilon$ module, the condition posed on both walls is the use of wall functions. The wall functions operate as explained in section 2.2.3. For the Algebraic yPlus module the no-slip condition is posed on both walls, meaning that $\vec{u} = 0$ at the wall.

7. Boundary condition - Boundary 7 functions as the inlet for the molten salt flow. The inlet boundary conditions consist of a inlet velocity profile and initial values for the turbulence variables. When regarding the turbulence variables, the initial values of k and ϵ for the $k-\epsilon$ module are calculated using equation 2.13 and initially equal $k_{in} = 1.84 \times 10^{-3}\,\mathrm{m^2\,s^{-2}}$ and $\epsilon_{in} = 2.88 \times 10^{-3}\,\mathrm{m^2\,s^{-3}}$. For the Algebraic yPlus model, the value for the mixing length l_{mix} and the y^+ value of the first computational node are to be specified. For l_{mix}, similarly as in

the calculation of ϵ_{in}, a value of $0.03H$ is assumed [18]. Since [16] prescribes at least three computational nodes to be placed in the viscous sublayer, for which $y^+ < 5$, the first node is placed at $y^+ = 0.9$.

8. Boundary condition - This boundary serves as the outlet for the molten salt flow. Since the flow should be fully developed, only flow perpendicular to the boundary is permitted. With RANS modelling, a fully developed flow only has a velocity component in the streamwise direction [16].

3.2.4 Mesh creation

Successful mesh creation relies on a balance of two properties of the mesh. First and foremost, the mesh should be dense enough to produce accurate results. Secondly, a limited computation time is desired, since this is largely correlated to the mesh density, this should be taken into account when creating a mesh. In short, an optimal balance is reached when a mesh is just dense enough so it does not influence the results of the model. Next to achieving this balance, the meshing requirements for the $k - \epsilon$ and the Algebraic yPlus module are also dissimilar.

$k - \epsilon$ module mesh

For the $k - \epsilon$ module the approach of reaching the balance mentioned above constituted of running the same calculation with increasing mesh density. Since the model uses wall functions, the exact configuration of the mesh near the wall is somewhat less relevant, so the physics-controlled meshing option was chosen. By choosing this option, COMSOL constructs a suitable mesh for the physics modules selected by using a combination of free triangular and boundary layer mesh elements. Figure 3.5 demonstrates a qualitative comparison of a physics-controlled mesh and a user-controlled mesh.

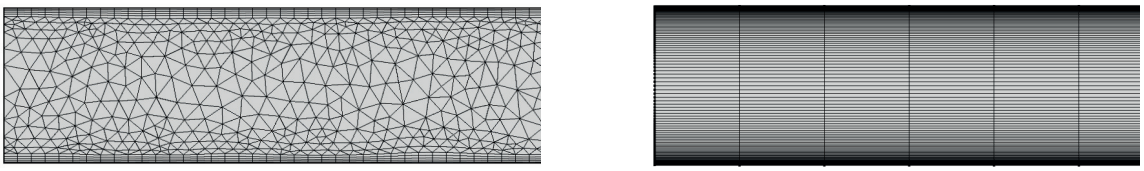

(a) Physics-controlled (b) User-controlled

Figure 3.5: Comparison of a physics-controlled and a user-controlled mesh configuration

For the determination of the accuracy of the mesh, the velocity profile was used as a reference. In figure 3.6, an analysis is provided for physics-controlled meshes of different densities and their performance in calculating the velocity profile. From figure 3.7a, it can be deduced that the lower mesh densities have their effect on the calculation of the velocity profile, simply because the velocity profile is rather jagged. This implicates that the mesh is still too rough, since a realistic velocity profile should be smooth. When looking at figure 3.7b, it is gathered that from $140 \cdot 10^3$ mesh elements and up, the profile is smooth and does only differ slightly when compared to the profile calculated with $440 \cdot 10^3$ elements, indicating that $140 \cdot 10^3$ elements is dense enough for a physics-controlled mesh.

Since the computation time for a mesh of $140 \cdot 10^3$ elements is still rather long, the user-controlled mesh is also investigated for the $k-\epsilon$ module. Figure 3.7 presents the analysis for the user-controlled meshes. From the figure, it can be deduced that the curve is continuous from a mesh density of $38 \cdot 10^3$ mesh elements, and subsequently the results do not differ. The initial assertion that a physics induced mesh would better suit the $k-\epsilon$ model should therefore be rejected, and the use of a user-controlled mesh of 38×10^3 elements is preferred.

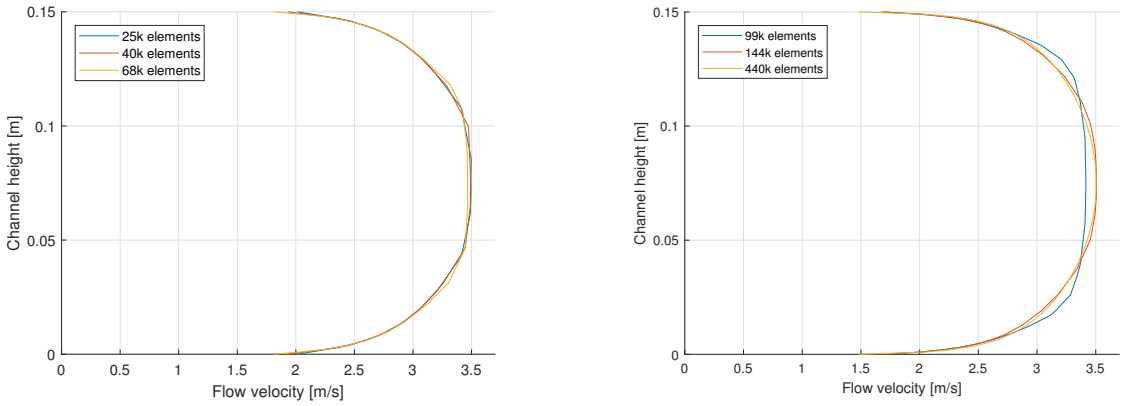

(a) Lower mesh densities.

(b) Higher mesh densities.

Figure 3.6: Velocity calculations with physics-controlled meshes.

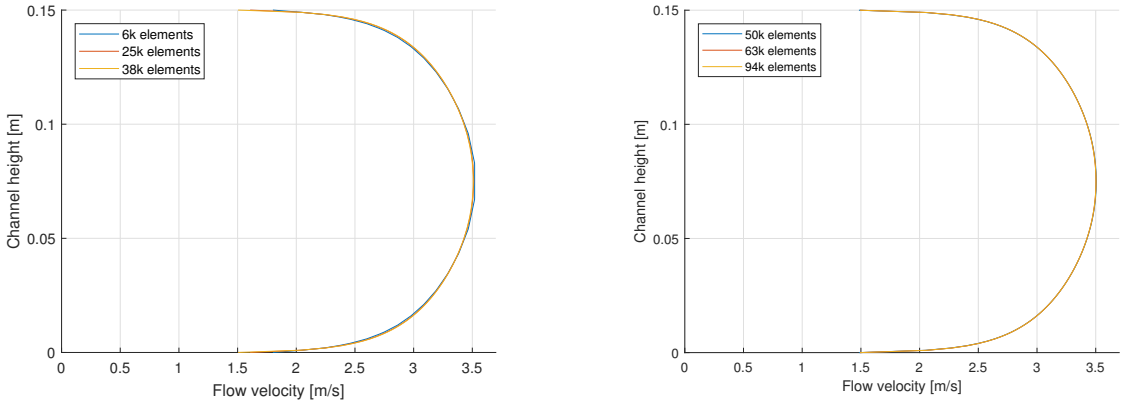

(a) Lower mesh densities.

(b) Higher mesh densities.

Figure 3.7: Velocity profile calculations with user-controlled meshes.

Algebraic yPlus module mesh

Since the module does not use wall functions, the mesh configuration near the wall is of the highest importance for the accuracy of the model. As stated before, Wilcox [16] recommends a minimum of three computational nodes in the viscous sublayer for accurate results. In order to satisfy this, the first computational node is set at $y^+ = 0.9$. Using the equations 2.14, 2.16, 2.33 and 2.36, the following y value can be found for $y^+ = 0.9$:

$$y = \frac{y^+ \nu}{u_\tau}, \quad u_\tau = \sqrt{\frac{\tau_{wall}}{\rho}}$$

$$\tau_{wall} = \frac{1}{2} c_f \rho U_0^2, \quad c_f = 0.0205 Re_\delta^{-1/6}$$

Since Re_δ is known, c_f can be calculated, which can then in turn be used to calculate τ_{wall}, since the density ρ and the free flow velocity U_0 are known. Lastly, the friction velocity u_τ is solved for, which is used to compute the corresponding y value for $y^+ = 0.9$. All of this leads to a y value for the first computational node of y= $1.327 \cdot 10^-5$ m. When $y^+ = 5$ is taken, it can be calculated that the viscous sublayer reaches to a height of y = $7.374 \cdot 10^-5$, in which three computational nodes should be present.

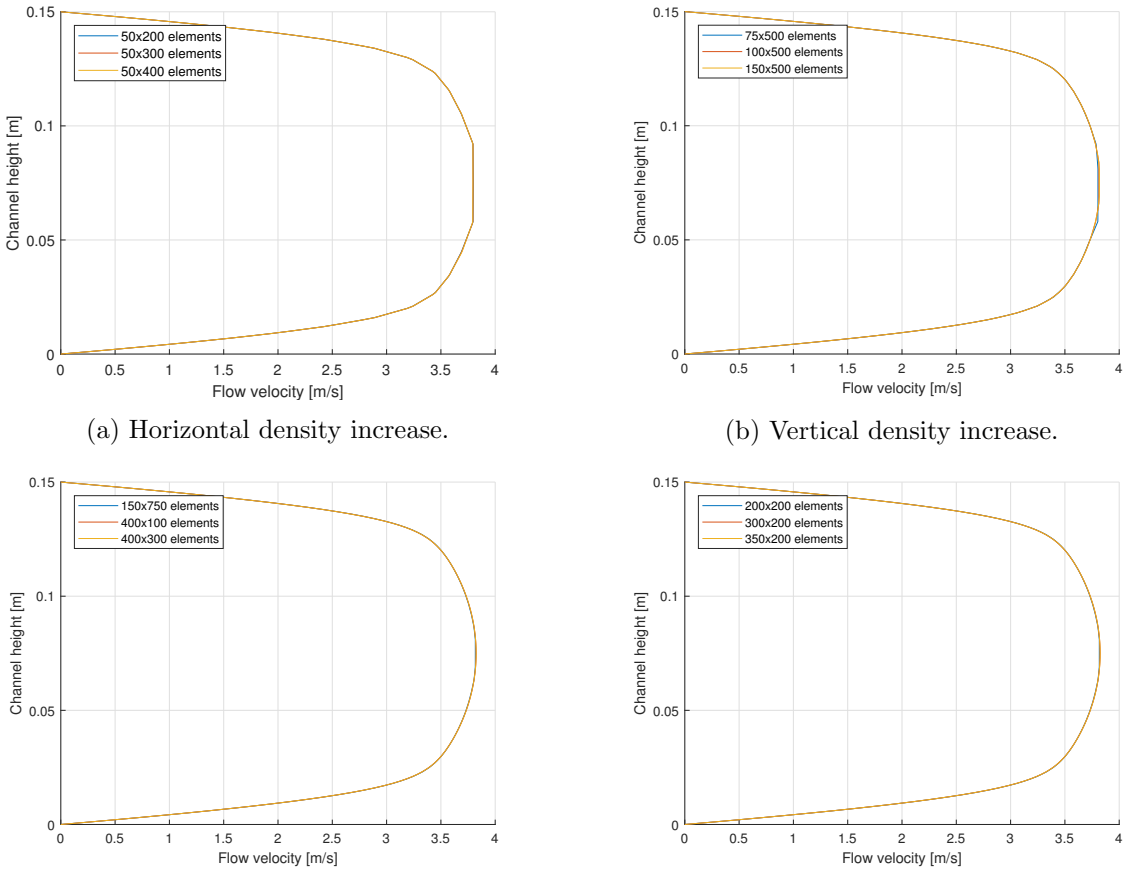

(a) Horizontal density increase.

(b) Vertical density increase.

(c) High density calculations.

(d) Balanced mesh densities.

Figure 3.8: Velocity calculations with user-controlled meshes.

To account for this, a user-controlled mesh is constructed. In the horizontal direction, an even distribution for the computational nodes is appointed. In the vertical direction, the boundary layer should be accounted for. This is done by selecting a symmetrical and geometrical distribution for the computational nodes, with the smallest cell being the most outer ones with a height of $1.327 \cdot 10^{-}5$ m. The geometrical distribution is set up so that the largest cell in the center of the channel has a significantly larger height than the smallest cell at the wall. Figure 3.5 clearly shows an example of the difference in vertical size of the cells near the wall in a user-controlled mesh.
Equally as with the $k - \epsilon$ module, a mesh analysis is performed to retrieve the most accurate mesh with the least mesh elements. Figure 3.8 provides the results of said analysis. User-controlled meshes are constructed by selecting the number of horizontal and vertical mesh elements. As stated, the smallest mesh elements have a restricted size due to the viscous sublayer. For all meshes in the analysis, this was accounted for by altering the ratio of smallest to biggest mesh element size.

Starting the interpretation of the analysis in figure 3.8, it can be gathered from 3.8a that a decrease in the number of horizontal mesh elements to as low as 200 does not influence the model calculations, as all of the velocity profiles are identical. The number of vertical elements, however, does influence the calculation, as figure 3.8b shows. With an increasing number of vertical mesh elements, the curve converges to a continuous one. By closely studying figures 3.8c and 3.8d is can be concluded that a mesh of 200 horizontal and 200 vertical elements bring forth an accurate result, which does not differ with increasing mesh density and is therefore the most suitable for models using the Algebraic yPlus module.

3.2.5 Computation and post-processing

When the mesh is built, COMSOL is able to start the computation of the model. The computation is guided by the study type that is defined. To simulate the normal operating conditions of the MSFR, the stationary solution of the system is of interest, so the stationary computation study is selected. Afterwards, a myriad of options exist within COMSOL to express the results, such as various plots, tables and multi-dimensional graphs. For this thesis, the desired values are collected from COMSOL by using the 'derived values' option. By using this option, the selected values are exported in a format, which is loaded in by MATLAB. Subsequently, MATLAB is used for the actual post-processing of the data and the generation of the various graphs and tables. The relevant MATLAB scripts are included in Appendix B.

3.3 COMSOL models

Now that the entire workflow of COMSOL is discussed, the actual models themself are specified. An overview of all the models that have been attempted to run is found in Appendix C. As can be seen, more than 50 models have been used throughout this thesis, most of which were unsuccessful in running properly. Most striking is the amount of 3D models that saw the light of day. The reason for this is that somewhat later in the project, the added value of a 3 dimensional model was questioned when compared to a 2 dimensional model. The rationale behind the decision to pursue the 2 dimensional approximation was already given in section 2.2.5., so in this section, only the models that were actually used for their results are discussed. The models will be discused by their goals and by the way their configurations differ from the standard one as represented by figure 3.1. The abbreviations BC's and IV's refer to the boundary conditions and initial values respectively.

3.3.1 Model 1a and 1b: Establishing the velocity profile

- Goal: Defining the fully developed velocity profile and the accompanying turbulence variable profiles of k and ϵ.
- Geometry: $\mathrm{L_{chann}} = 40\,\mathrm{m}$. The hugely increased channel length is to ensure a fully developed profile downstream.
- Physics: (a) $k-\epsilon$ turbulent flow module, (b) Algebraic yPlus turbulent flow module.
- BC's & IV's: Uniform inlet velocity U_{in}=3.2 m/s and turbulence variables at inlet
  (a) k_{in}= $1.84 \cdot 10^{-}3\ \mathrm{m^2/s^2}$ and ϵ_{in} =$2.88 \cdot 10^{-}3\ \mathrm{m^2/s^3}$
  (b) $l_{mixing} = 0.03H = 0.0045\,\mathrm{m}$ and $y^+ = 0.9$

3.3.2 Model 2a and 2b: Determination of the volumetric cooling power $P_{cooling}$

- Goal: Retrieve the cooling power $P_{cooling}$ for the dimensions as put forth by table 2.2
- Geometry: Dimensions are taken from table 3.1.
- Physics: (a) $k-\epsilon$ turbulent flow module, (b) Algebraic yPlus turbulent flow module.
  (a,b) Non-isothermal flow module, heat transfer module.
- BC's & IV's: (a) Inlet velocity profile and k and ϵ profiles as generated by model 1a
  (b) Inlet velocity profile and y^+ and l_{mix} value as generated by model 1b
  (a,b) Parameter sweep for $P_{cooling}$ to determine its value.

3.3.3 Model 3a and 3b: Influence of D_{plug} on cooling requirements

- Goal: Determine the influence of D_{plug} on the cooling requirements
- Geometry: Dimensions are taken from table 3.1.
- Physics: (a) $k-\epsilon$ turbulent flow module, (b) Algebraic yPlus turbulent flow module.
  (a,b) Non-isothermal flow module, heat transfer module.
- BC's & IV's: (a) Inlet velocity profile and k and ϵ profiles as generated by model 1a
  (b) Inlet velocity profile and y^+ and l_{mix} value as generated by model 1b
  (a,b) Parameter sweep for D_{plug} to observe its impact on the cooling requirements.

3.3.4 Model 4a and 4b: Influence of F_{plug} on cooling requirements

- Goal: Determine the influence of F_{plug} on the cooling requirements
- Geometry: Dimensions are taken from table 3.1.
- Physics: (a) $k-\epsilon$ turbulent flow module, (b) Algebraic yPlus turbulent flow module.
  (a,b) Non-isothermal flow module, heat transfer module.
- BC's & IV's: (a) Inlet velocity profile and k and ϵ profiles as generated by model 1a
  (b) Inlet velocity profile and y^+ and l_{mix} value as generated by model 1b
  (a,b) Parameter sweep for F_{plug} to observe its impact on the cooling requirements.

Chapter 4

Results and discussion

In this chapter, the results of the various COMSOL models are presented and discussed. The first model, as explained in the previous chapter, is aimed at capturing the fully developed velocity profiles and the corresponding turbulence variables. The results are afterwards used in all the ensuing models. All graphs that are presented here are composed in MATLAB [21].

4.1 Establishing the developed velocity profile

The requirement to establish the fully developed velocity profile in the channel was identified in section 2.1.2. Because the molten salt is pumped through the re-circulation zone before it traverses the freeze plug surface, it has already developed a velocity profile. The velocity profile has a large impact on the heat transfer of the molten salt flow to the freeze plug, as was shown in section 2.3. In section 3.1 the simplifications of the geometry of the models were addressed, which for the main part had to do with the artificial creation of a pure channel flow by straightening both reactor walls.
Model 1a and 1b are dedicated to finding the fully developed velocity profiles and the corresponding turbulence variables, both for different turbulence modules. It does so by developing a velocity profile over a channel of 40 m from a uniform inlet velocity U_{in}= 3.2 m/s. Their results, as mentioned, will be transferred to the subsequent models in order to simulate a developed profile, as would be present during normal operating conditions of the MSFR.

4.1.1 Model 1a: $k-\epsilon$ velocity profile

The length of the channel in the geometry of model 1a, L_{chann}, was taken to be equal to 40 m, with the assumption that the velocity profile would have set in by the end of the channel. It turns out, that for model 1a, the profile is developed after 20 m. Figures 4.1, A.1a and A.1b, of which the last two are found in appendix A, demonstrate the average flow velocity U and both turbulence variables k and ϵ over the entire length of the channel, and it is easily gathered that the flow is fully developed after 20 meter, since all of the slopes for the variables equal zero after the flow has passed the 20 meter mark. The developed velocity and turbulence variables profiles can therefore be retrieved at any point past 20 meters into the channel.

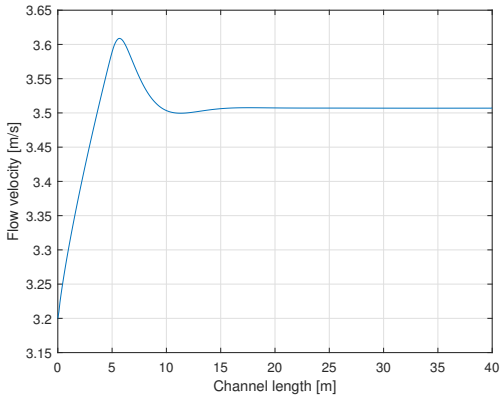

Figure 4.1: Downstream average flow velocity U in the middle of the channel at y= 0.075 m.

Figures 4.2, 4.3b and 4.3a present the fully developed flow profile, including the associated turbulence variables. The use of wall functions of the $k-\epsilon$ model is clearly visible here, as all profiles in reality would be zero at a no-slip wall, since $\overline{u} = u' = 0$ there. The fact that the velocity, for instance, is non-zero does provide insight in the nature of the wall functions employed. As explained in section 2.2.3., wall functions model the flow near the wall from a certain y^+ value, that is in the log-law layer. Using the flow velocity magnitude figure 4.2 models at the wall of approximately 1.5 m/s, the y^+ and the corresponding y value that the wall functions start from can be calculated. Using equation 2.14 and the law of the wall, equation 2.17, this yields:

$$u^+ = \frac{u}{u_\tau} = \frac{1.5}{0.124} = 12.1$$

$$u^+ = \frac{1}{0.41}\ln\left(y^+\right) + 5.1$$

Which leads to $y^+ = 17.4$, which would indicate that COMSOL models its first computational node right in or just before the beginning of the log-law layer. The motivation for this calculation, however, stems from the fact that the corresponding y value, using equation 2.14, is equal to $3.44 \cdot 10^{-}4$ m, effectively creating a layer of insulation between the molten salt flow and the freeze plug. The results of the other models will prove if this potentially threatens accurate modelling of the heat transfer.

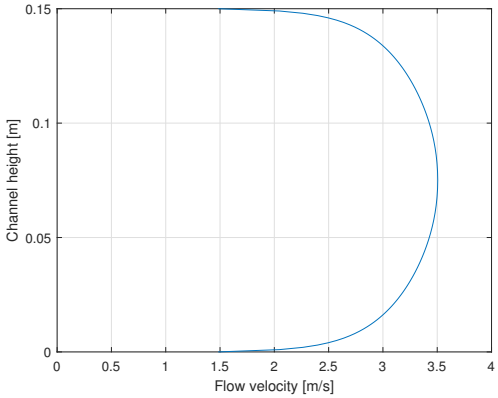

Figure 4.2: Developed flow velocity profile as present at L_{chann}=20 m.

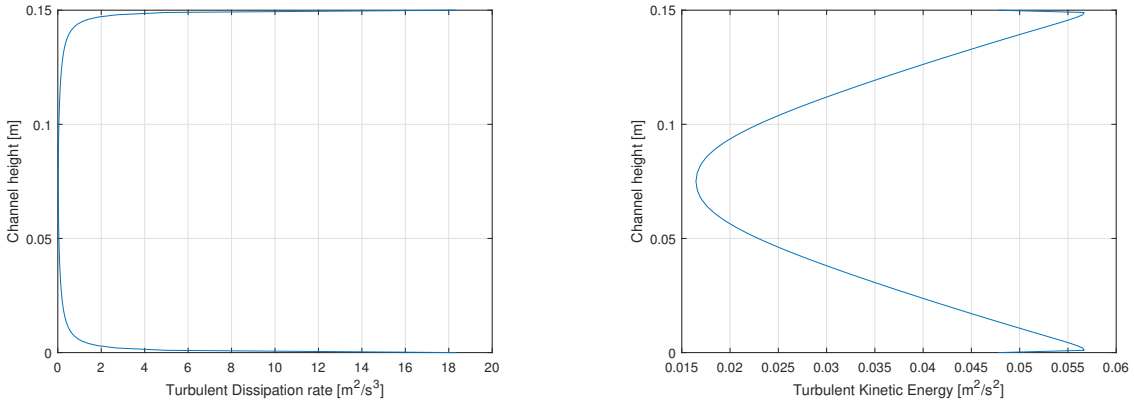

(a) Developed ϵ profile.

(b) Developed k profile.

Figure 4.3: Developed turbulence variable profiles as present at L_{chann}=20 m.

The profile of ϵ in figure 4.3a can be explained qualitatively by recalling that it was a measure for the amount of turbulent kinetic energy that is dissipated as thermal internal energy. The closer to the wall, the larger the wall shear stress τ_{wall} becomes, which contributes greatly to the dissipation of kinetic energy into thermal internal energy. The profile of k is understood by pointing out that the production of k is proportional to the derivative of the free flow velocity in the lateral direction, as specified in equation 2.9. This means k is primarily produced from the free bulk flow in the direction perpendicular to it, which clarifies the 'm'-shaped profile.

4.1.2 Model 1b: Algebraic yPlus velocity profile

Model 1b basically holds the same goals as model 1a, and so its execution came to pass quite identically. Initially, the length of the channel was also taken to be 40 meters. The resulting downstream average flow velocity in the middle of the channel at $y = 0.075$ m is plotted in figure 4.4. From this, it is deduced that the developed velocity profile already settles in around 5 meters into the channel.

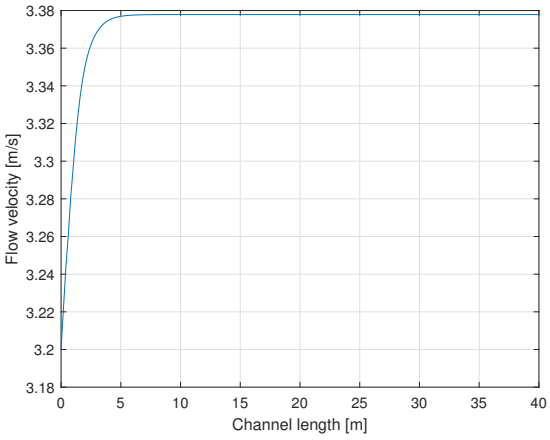

Figure 4.4: Downstream average flow velocity U in the middle of the channel at y=0.075 m

.

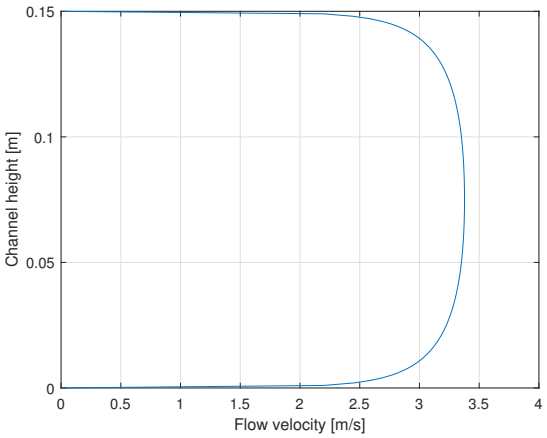

Figure 4.5: Developed flow velocity profile as present at L_{chann}=5 m.

From figures 4.5 and 4.4 it is immediately noted that the Algberaic yPlus module does not use wall functions since the flow velocity is zero at the wall. Is is striking that the Algebraic yPlus module achieves the developed velocity profile 4 times faster than the $k-\epsilon$ module. An explanation for this could be the direct modelling of the μ_T from the wall up instead of through secondary turbulence variables as k and ϵ. The velocity profile as displayed in figure 4.5 also compares better to the values from literature, with a steeper segment near the wall and a more flattened bulk velocity segment than in figure 4.2. This is also due to the Algebraic yPlus module being able to compute the flow near the wall, as this is where the highest velocity gradients arise [18].

The resulting velocity and turbulence profiles of both model 1a and model 1b are post-processed in MATLAB. Not only is MATLAB used to generate the plots, but the data from COMSOL is also used to generate an analytical fit for the profiles using the Curve Fitting Tool functionality. Each analytical fit, usually a higher order rational polynomial or a Fourier series representation, is subsequently transferred with the corresponding fit parameters to future models. This way, future models have the developed velocity profile defined at their inlet, and are the normal operating conditions of the MSFR replicated. The MATLAB scripts that were used for the generation of the plots and for the fitting of the profiles are adopted in Appendix B. The polynomials and Fourier series representations that were used to transfer the velocity profiles to subsequent models are also found in Appendix B.

4.2 Determination of the volumetric cooling power $P_{cooling}$

As defined in chapter 3, the cooling power $P_{cooling}$ is modelled by a volumetric heat sink assigned to the Hastelloy N. The same criteria for the determination of a suitable $P_{cooling}$ were used for both model 2a and model 2b. A suitable volumetric cooling power is defined as a cooling power, for which at least 95% of the CsCl of the plugs is in the solid state. This assertion is based on that fact that the CsCl in COMSOL was modelled to be a solid and to ensure that the freeze plugs remained attached to the Hastelloy N plug module securely. First, the resulting cooling powers and the particular findings per model are presented and discussed. Afterwards, their findings are compared and the suitability for simulating the molten salt flow is evaluated for both models.

4.2.1 Model 2a: $k - \epsilon$ cooling power

To identify a suitable $P_{cooling}$, a parameter study was performed in COMSOL, gradually increasing the value in order to retrieve the optimal value. Figure 4.6a shows the initial and investigative parameter study. In the figure, the temperature of both the molten salt flow and the freeze plug is presented. It is clear that with increasing $P_{cooling}$ the temperature profile decreases more sharply. The melting temperature of the freeze plug material, CsCl, is also adopted. In this thesis, the assertion is made that the CsCl melts and becomes liquid when the temperature of the solid CsCl becomes larger than T_{melt}.

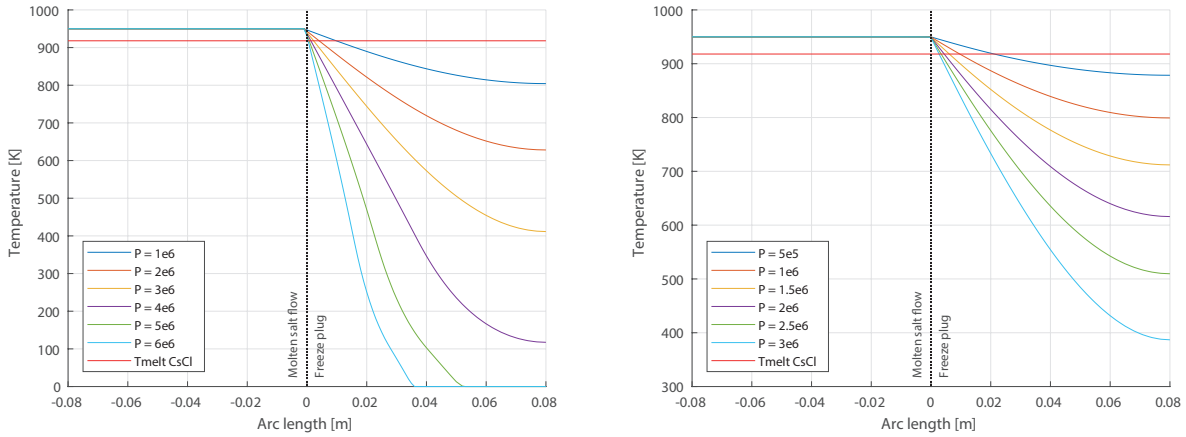

(a) Initial $P_{cooling}$ parameter sweep.

(b) Refined $P_{cooling}$ parameter sweep.

Figure 4.6: Temperature profiles in molten salt flow and freeze plug for different volumetric cooling powers. The unit of P is [W/m^3].

It is noted that the investigative study of figure 4.6a employs a range of parameters for $P_{cooling}$ that extends too far. When examining the temperature profile that is induced by P = 6 MW/m^3, it is learned that more than half of the freeze plug is at 0 K, which, surely, is not desirable, partially because of the longer melting time of the plug in case of an emergency. The curve profile for P = 1 MW/m^3, however, has its intersection with the melting temperature around x = 0.01 m, causing a significant part of the plug to be in liquid form, and therefore not passing the 95% requirement. To further investigate the most suitable $P_{cooling}$, a more refined parameter study was performed.

In figure 4.6b, the results of the refined study are presented. When lowering the value of $P_{cooling}$, the temperature profile of the molten salt flow penetrates deeper in the freeze plug, effectively moving the intersection with the melting temperature further into the plug, causing for a greater portion of the freeze plug to be in a liquid state. As stated, the suitability criterion in this thesis is taken to be that 95% of a freeze plug is in its solid state. To investigate the evident relation between the cooling power and the percentage of the plug in its solid state, a meticulous parameter sweep of $P_{cooling}$ was performed. Its results are on display in figure 4.7.

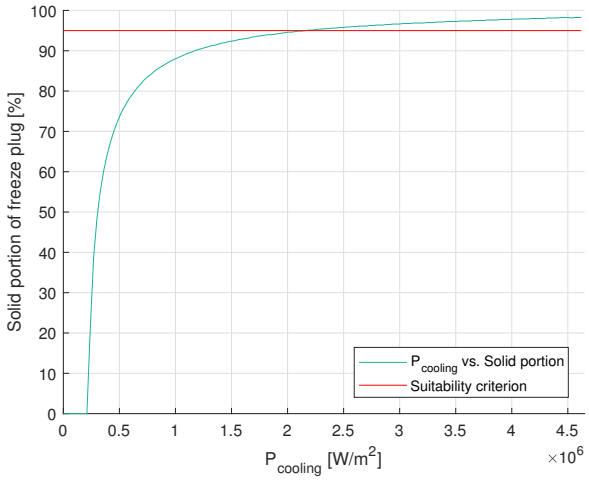

Figure 4.7: Relation of percentage solid freeze plug material and $P_{cooling}$.

It is observed that for low values of $P_{cooling}$, the complete freeze plug is molten and no solid portion remains. Then, a small increase in cooling power relates to a rapid increase in the solid portion of the freeze plug. Eventually, figure 4.7 shows that the 95% threshold is reached with a cooling power of 2.1 MW/m^3. It should be noted, however, that $P_{cooling}$ is a volumetric cooling power. Using the following relations, it is possible to translate $P_{cooling}$, assigned to the Hastelloy N in the module, to the total cooling power P_{total} of a freeze plug module.

$$P_{total} = V_{Hastelloy} \cdot P_{cooling} \tag{4.1}$$

$$V_{Hastelloy} = V_{module} \cdot R_{Hastelloy} \tag{4.2}$$

$$R_{Hastelloy} = \frac{A_{Hastelloy}}{A_{Hastelloy} + A_{plugs}} \tag{4.3}$$

In which $V_{Hastelloy}$ is the total volume of Hastelloy N in the 3D plug module. The volume is calculated by multiplying the total module volume V_{module} by $R_{Hastelloy}$, the portion of Hastelloy present in the 2D representation. Equation 4.2 contains the assumption that the portion of Hastelloy is the same in the 3D plug volume as is it in the 2D cross section of the models. Figure 4.8 is the results of the translation to the total cooling power for model 2a.

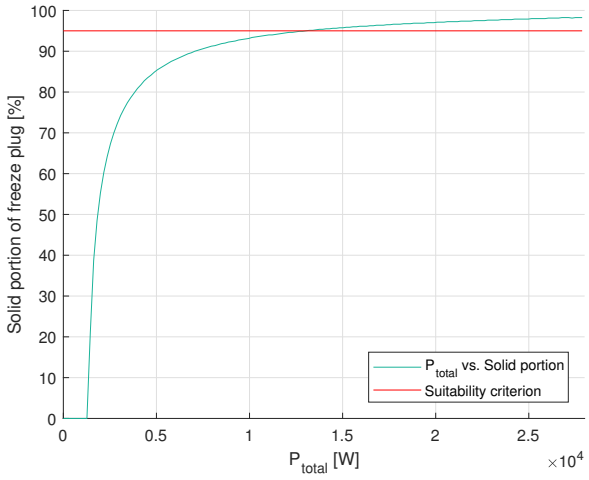

Figure 4.8: Relation of total cooling power P_{total} and solid % CsCl.

The results of the figure indicate that the plug module is sufficiently cooled for a total cooling power P_{total} value of 12.7 kW.

4.2.2 Model 2b: Algebraic yPlus volumetric cooling power

The execution of determining the volumetric cooling power for the Algebraic yPlus module in model 2b was quite similar to model 2a. First, an investigating parameter study was performed, with the same range for $P_{cooling}$ as in figure 4.6a. The results are on display in figure 4.9a. Again, the initial range for $P_{cooling}$ was too broad and extended too far, resulting in parts of the plug at 0 K for higher values of $P_{cooling}$. The refined parameter study is presented in figure 4.9b, and at first glance, seems to portray the same situation as figure 4.6b, but by close examination is it noted that the profiles are not entirely similar.

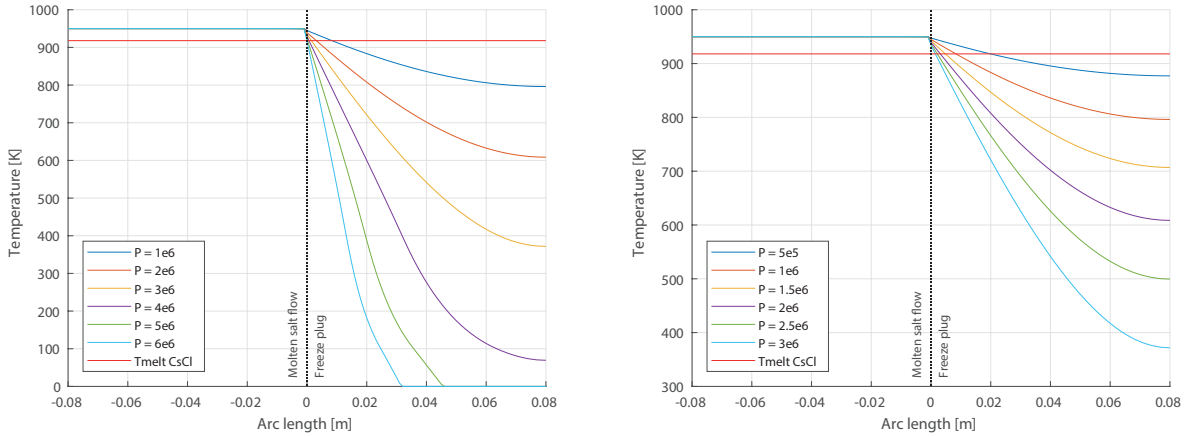

(a) Initial $P_{cooling}$ parameter sweep.

(b) Refined $P_{cooling}$ parameter sweep.

Figure 4.9: Temperature profiles in molten salt flow and freeze plug for different cooling powers.

To emphasize the differences and in order to visualize the Algebraic yPlus $P_{cooling}$ and solid portion relation, the same analysis as put forth in figure 4.7 was performed. Figure 4.10 features the results

of said analysis.

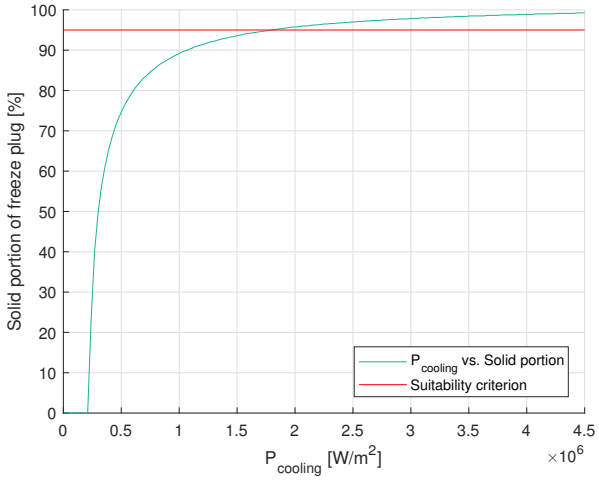

Figure 4.10: Relation of percentage solid freeze plug material and $P_{cooling}$.

In figure 4.10, the same qualitative behaviour of the relation is noted. The intersection, however, with the suitability criterion manifests itself for a different $P_{cooling}$ value. For the Algebraic yPlus module, the criterion is met for a cooling power upward of 1.8 MW/m^3. The same translation to the total cooling power P_{total} as performed for model 2a can be used for model 3b as well, of which the results is displayed in figure 4.11.

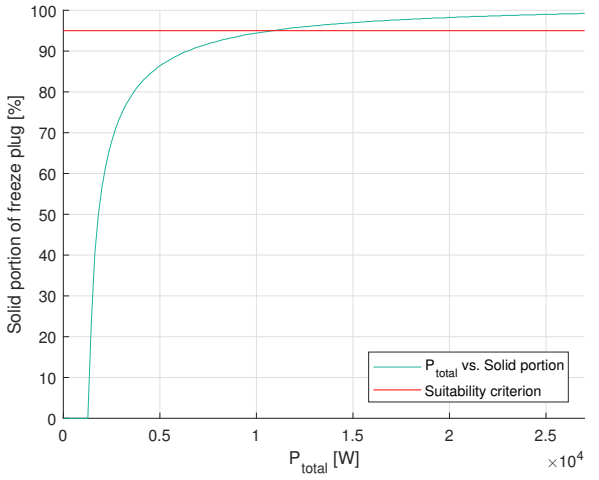

Figure 4.11: Relation of total cooling power P_{total} and % solid CsCl.

From the plot, it can be gathered that the plug module is sufficiently cooled for a P_{total} of 10.9 kW.

From studying the parameter studies and relations presented of both models, several intermediate remarks can be made:

- The results of both models are qualitatively comparable. The results are, however, quantitatively somewhat dissimilar. This could suggest that the use of wall functions for the configuration of molten salt flow and freeze plug is a robust but less accurate alternative to using the Algebraic yPlus module.
- The reasons for the dissimilarity in the resulting suitable values of $P_{cooling}$ could be retrieved by investigating the boundary layer near the flow plug interface more intimately, because it is the area in which the two models differ their representation of the molten salt flow. As such, a near-wall analysis could provide insight in the differences in heat transfer and explain the different $P_{cooling}$ values.
- At first sight it strikes as if the molten salt flow is not influenced by $P_{cooling}$, since the temperature profile in the molten salt flow remains at a constant temperature of 950 K, even at increased values for $P_{cooling}$. From the figures, it can be concluded that the temperature of the bulk of the molten salt flow, beyond the log-law layer, is not influenced by $P_{cooling}$. The influence it bears on the boundary layer, however, is not made visible in the analyses put forth. An additional investigation of the boundary layer is needed to bring clarity to the matter.
- When regarding that the MSFR features 16 plug modules in its design, the resulting values for P_{total} of 12.7 kW and 10.8 kW per plug module are desirable, in the sense that the total cooling power for all the plugs would amount to 203 kW and 172 kW, for $k-\epsilon$ and Algebraic yPlus subsequently. Assuming a MSFR energy capacity of 1000 MW, which is not uncommon for current Plutonium based reactors, cooling the freeze plugs would only take up 0.0203 % and 0.0172 % of the energy production for models 2a and 2b, respectively.

4.2.3 Near-wall investigation of model 2a and model 2b

As remarked, the resulting values for the total cooling power P_{total} differ to some extent for models 2a and 2b. The main distinction between both models is the use of wall functions for the $k-\epsilon$ model to compute the flow near the wall. From model 1a it was gathered that the first computational node of the $k-\epsilon$ model is placed at a y^+ value of 17.4, corresponding to a y value of $3.44 \cdot 10^{-}4$m. Placing the first node at $y^+ = 17.4$ means the model skips the laminar sublayer and the buffer layer, as figure 2.4 shows. In this section, the influence of using wall functions on the heat transfer from the plug to the laminar sublayer is investigated.
Before all else, model 2a with wall functions is examined. Figure 4.6 suggested that the temperature of the molten salt flow was not affected by the cooling power in the plug, even for high volumetric cooling powers in the range of 5e6 W/m^3. For high values of $P_{cooling}$, the figures displayed that the freeze plug is solid for 99% and that the entirety of the molten salt flow remained at 950 K. Figure 4.12 portraits the temperature profile in the boundary layer, up to a y^+ value of 17.4, for two different high cooling powers, of respectively 2 and 4 times the required volumetric cooling power.

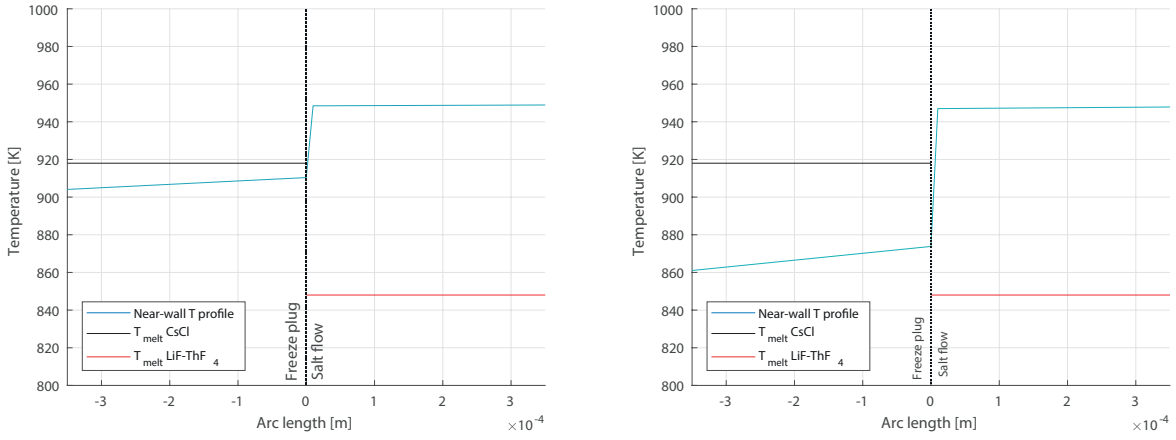

(a) $P_{cooling}$=5 MW/m^3. (b) $P_{cooling}$=10 MW/m^3.

Figure 4.12: Model 2a: Temperature profiles in boundary layer and plug module.

The melting temperatures of the freeze plug material and the molten salt are also plotted in figure 4.12 to shed light on the situation in the boundary layer. It is noted that the temperature of the molten salt does not come near its melting temperature and is effectively in both figures at a constant temperature of 950 K. This is understood by remembering that the wall functions model a flow velocity of 1.5 m/s at the wall. Because of this, the advective heat transport of the incoming LiF-ThF_4 at the wall heavily outweighs the cooling power of the freeze plug. From figure 4.12a it is learned that the temperature of the plug surface T_{surf} equals 910 K. By using equation 2.30, the convective heat flux from the molten salt through the plug surface can then be calculated by taking the difference between the bulk temperature of 950 K and the surface temperature of 910 K, resulting in a convective heat flux $q"_{conv}$ = 387 kW/m^2.
The reason the molten salt flow does not experience much of a temperature difference, however, is because the advective heat flux that the molten salt flow carries with it, far outweighs the flux induced by the cooled plug surface. For a flow velocity of 1.5 m/s, the advective heat flux that the molten salt flow transports in the streamwise direction is in the order of 10^{10} W/m^2 when traversing the plug module. It can therefore be concluded that because of the modelled flow velocity at the wall by using the wall functions, the molten salt flow is not influenced by the cooling power of the plug module.
Model 2b does not model a flow velocity near the wall, as can be gathered from figure 4.5, leading to the expectation that the advective heat transfer does not play a significant role in the boundary layer, since the flow velocity is small there. Figure 4.13 displays the temperature profile in the region for a $P_{cooling}$ value of 5 MW/m^3 and 10 MW/m^3 respectively.

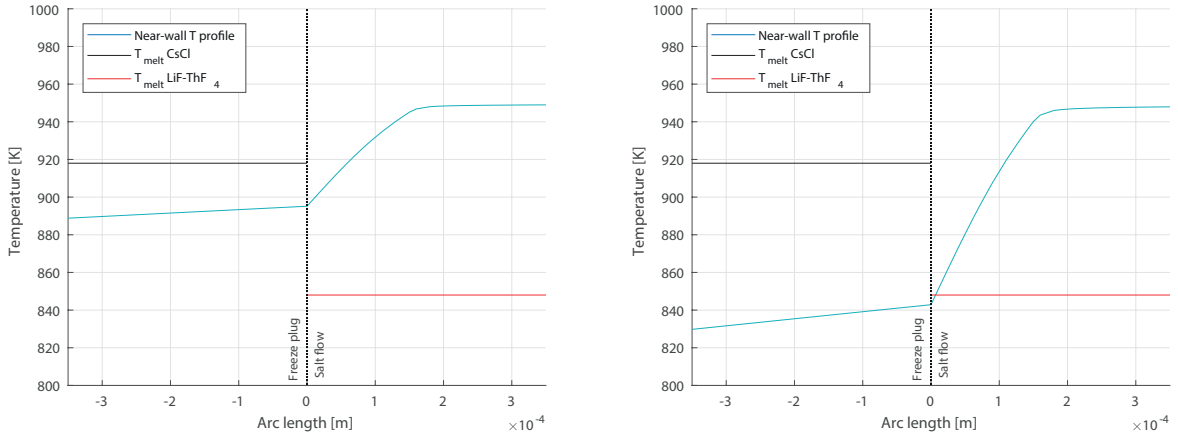

(a) $P_{cooling}$=5 MW/m^3 (b) $P_{cooling}$=10 MW/m^3

Figure 4.13: Model 2b: Temperature profiles in boundary layer and plug module above Hastelloy N section.

Comparing figure 4.13 to 4.12, it is immediately evident that the laminar sublayer is simulated in the Algebraic yPlus module, since the temperature profile develops more steadily in the molten salt flow. This signifies that in the laminar sublayer, the heat flux through the plug surface does exert an influence and is not trumped by the advective heat that is transported by the molten salt flow. Accordingly, it is noted that the plug surface temperature is lower than simulated by the $k-\epsilon$, which appears to be closer to reality, since the laminar sublayer will undeniably be influenced by the plug surface. With a more realistic surface temperature, a more realistic temperature profile in the plug is modelled and consequently more accurate cooling requirements are brought forward by the Algebraic yPlus module.
Although the correct modelling of the laminar sublayer does make the results of the Algebraic yPlus module more resembling of the actual operating conditions, the differences in the results are not insurmountable. Because of the enormouos advective flux generated by the molten salt flow relative to the heat flux through the plug surface, even when modelling the laminar sublayer, only a microscopic portion of the molten salt flow is influenced.
When including the melting temperatures of CsCl and LiF-ThF_4, several closing comments on the near-wall analysis can be put forward:

- The Algebraic yPlus module suggests to bring forward more accurate cooling requirements than the $k-\epsilon$ module, since is does model the influence of the cooled plug surface on the laminar sublayer. Consequently, since the temperature profile in the sublayer already experiences the negative heat flux through the plug surface, the Algebraic yPlus module produces lower plug surface temperatures. Lower plug surface temperatures result in a higher convective heat flux from the molten salt flow through the plug surface. The temperature profile in the plug, however, has a lower 'starting point' from the surface into the plug, which could clarify the lower cooling requirements found by model 2b compared to model 2a.

- The difference in the results of the turbulence models is, as remarked, significant for the cooling requirements because of the different plug surface temperatures they produce. However, since the advective heat flux is enormous compared to the induced flux by the plug surface, the molten salt flow is not influenced as much by the cooled plug surface. In both models, the molten salt flow regains its inflow temperature of 950 K before 0.2 mm into the channel.

- 0.2 mm represents a y^+ value of 10, so the entire laminar sublayer and part of the buffer layer are influenced by the cooled plug surface. Because of the combination of the strong advective flux and the relatively low melting temperature of the molten salt, it is learned that only with extreme volumetric cooling powers of over 4 times the necessary cooling power in the order of 1e7 W/m^3, solid layer of the molten salt flow could be formed on tpo of the cooled plug surface. Since the associated volumetric cooling powers are not relevant for suitable cooling requirements, it can be concluded that with appropriate volumetric cooling power, no solid LiF-ThF_4 sediment will be formed.

4.3 Geometry influence on cooling requirements

After identifying the appropriate values for both models of $P_{cooling}$ of $2.1 \cdot 10^6\, W/m^3$ and $1.8 \cdot 10^6\, W/m^3$ for the setup with dimensions as proposed by table 2.2, the influence of altering the geometry of the experimental setup is evaluated. In consideration of the geometry of the simulations as displayed in figure 3.1, and seeing as $P_{cooling}$ is a volumetric cooling power that only exists in the alloy plug module, the ratio of the freeze plug material CsCl and Hastelloy N, in which the cooling takes place, is paramount in determining the most suitable cooling requirements. The overall dimensions of the freeze plug module might also exert an influence on the cooling requirements.
The ratio of CsCl and Hastelloy N and the overall dimensions of the plug module, in the 2D approximation of this thesis, are influenced by a number of geometric parameters. Identified are D_{plug}, F_{plug}, D_{module} and H_{plug}. The diameter of the plug module D_{module} is assumed to be fixed at 0.4 m, based on the most current MSFR design as defined in [4]. The height of the freeze plugs and the plug module H_{plug} is based on previous research concerning the freeze plug by Swaroop [6] and van Tuyll [7] and is taken to be 0.08 m. The investigation of the height of the freeze plug module and its effects on the freeze plug stability are not within the scope of the present work.
In conclusion, the effects of the geometry on the cooling requirements are presented in this section. As determined, since the cooling power $P_{cooling}$ exists only in the Hastelloy N of the plug module, the ratio of CsCl and Hastelloy N is critical in determining the most suitable cooling requirements. The ratio is investigated by examining the effects of the plug diameter D_{plug} and the distance between adjacent freeze plugs F_{plug} more intimately.

4.3.1 Model 3a: Plug diameter influence with $k - \epsilon$ module

For the investigation of the effect of the plug diameter on the cooling requirements, several constraints were established. As stated, the module diameter D_{module} is fixed at 0.4 m because of the proposed MSFR design, dictating the allowed range for the freeze plug diameter. For the current model, the distance between adjacent freeze plugs F_{plug} is not varied and taken to be 0.1 m, in accordance with Makkinje [8] and Deurvorst [9]. From their work, it arose that optimal melting times are achieved by taking the adjacent freeze plug distance upwards of 0.06 m and a plug diameter that is at least two times smaller than the adjacent distance. For the analysis by model 3a and 3b, this would imply a maximum plug diameter of 0.05 m, when considering melting times. Since, however, the present work is dedicated to capturing the optimal cooling requirements instead of the fastest melting times, the freeze plug diameter is extended beyond 0.05, to investigate its effect on the cooling requirements more intimately. Figure 4.14 presents the geometrical setup used for the current analysis.

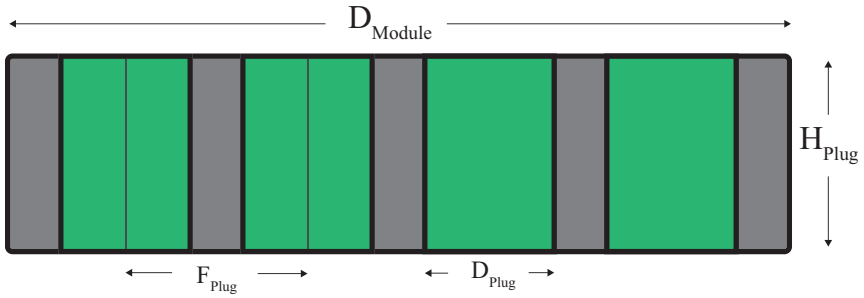

Figure 4.14: Detail of the setup used for models 3a and 3b, showing the plug module and its parametrisation.

The freeze plug diameter D_{plug} is varied from 0.01 m to 0.09 m in order to produce an extended range of measurements on the diameter influence. Figure 4.15a is the result of the initial parameter sweep for D_{plug}. It is evident that a small D_{plug} results in a small portion of the freeze plug to be above its melting temperature, since a small plug diameter implies a larger Hastelloy N to CsCl ratio and consequently more cooling occurs in the plug. The succeeding and more refined parameter sweep supports this assertion, as presented in figure 4.15b.

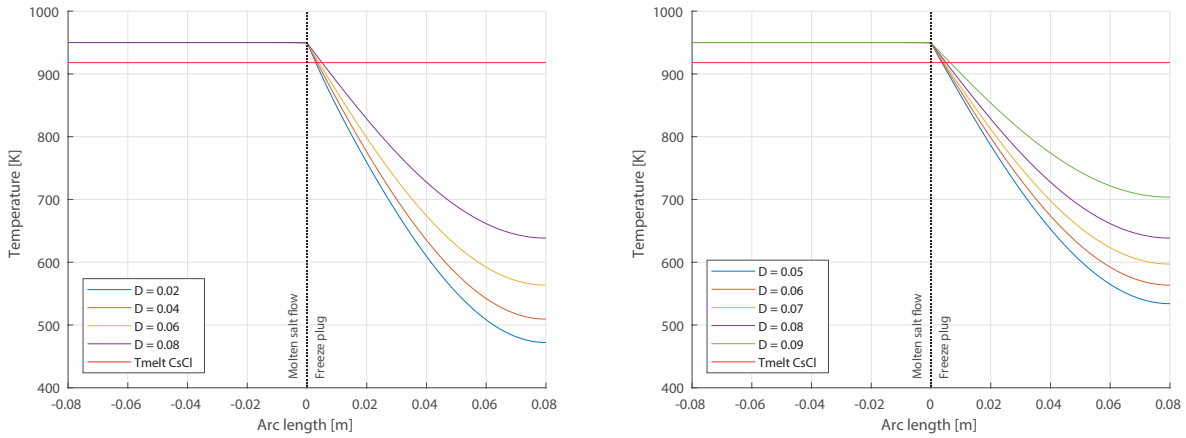

(a) Initial D_{plug} parameter sweep.

(b) Refined D_{plug} parameter sweep.

Figure 4.15: $k - \epsilon$ analysis on D_{plug} influence on cooling requirements.

In order to capture the freeze plug diameter influence more accurately, a meticulous parameter sweep is performed over a broad range of allowed plug diameters. Post-processing the results of said sweep in MATLAB allows for a visualization of the diameter influence on the percentage of solid freeze plug material with a cooling power $P_{cooling}$ of 2.5 MW/m^3, as shown in figure 4.16. The suitability criterion of 95% solid freeze plug material is also incorporated.

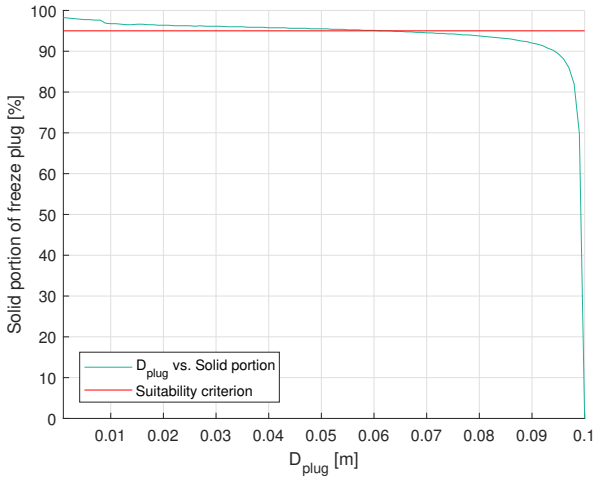

Figure 4.16: D_{plug} influence on percentage solid CsCl.

Figure 4.16 affirms the initial results of figure 4.15, namely the negative relation between the freeze plug diameter and the percentage solid freeze plug material. In the setup used of four freeze plugs adjacent at a distance of 0.1 m, a D_{plug} of 0.1 m would mean that there is no Hastelloy N left and thus the plug is not being cooled. This clearly results in a plug that is totally molten, as figure 4.16 clearly indicates. The suitability threshold of 95% solid material is reached for a D_{plug} of 0.061 m. Regarding the fact that a volumetric cooling power $P_{cooling}$ was used of 2.5 MW/m^3, equations 4.1 to 4.3 can be used to lay bare the relation of the total cooling power P_{total} and solid % of plug material based on the results of model 3a as displayed in figure 4.16. The figure below portraits the resulting relation.

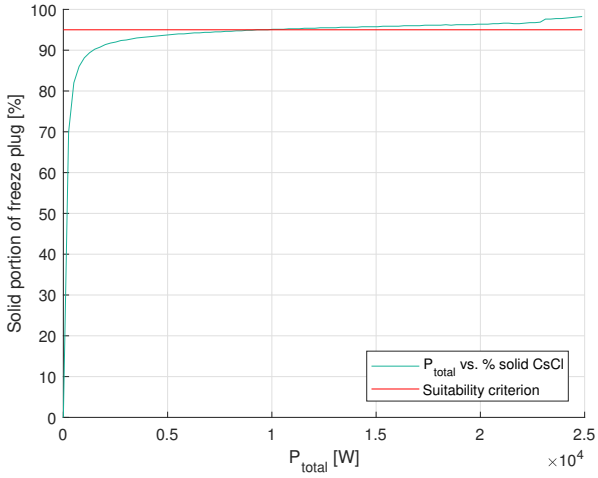

Figure 4.17: Model 3a relation between total cooling power P_{total} and percentage solid CsCl.

From the figure, it is noted that the suitability criterion is reached for a total cooling power P_{total} of 9.81 kW.

4.3.2 Model 3b: Plug diameter influence with Algebraic yPlus module

The D_{plug} influence analysis was conducted along the same lines as the one presented in the previous section. Initially, a rough sweep of D_{plug} is performed. From it, the most significant range for the freeze plug diameter is further explored. As was the case throughout the previous analysis, the range of the freeze plug in model 3b also extends from 0.01 m to 0.09 m.

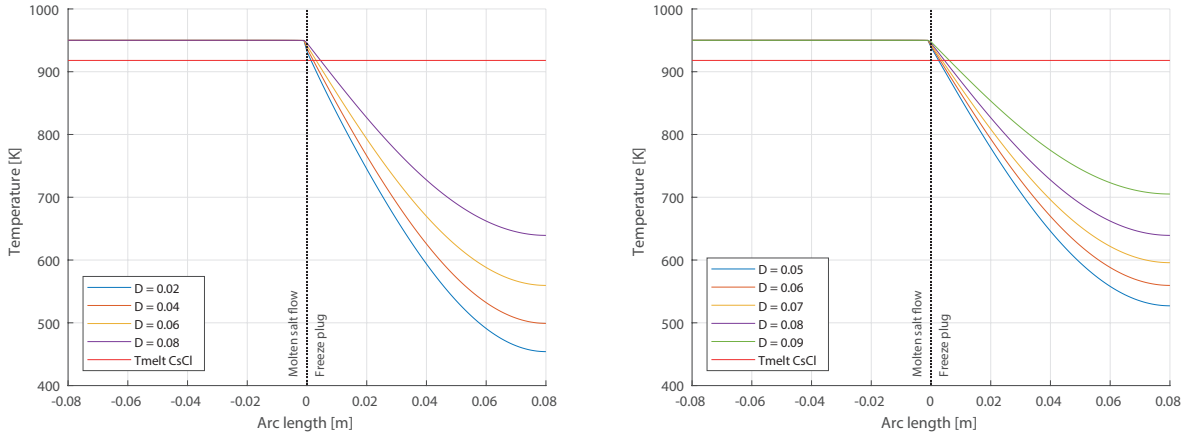

(a) Initial D_{plug} parameter sweep.

(b) Refined D_{plug} parameter sweep.

Figure 4.18: Algebraic yPlus analysis on D_{plug} influence on cooling requirements.

From figure 4.18 the relation between D_{plug} and the portion solid freeze plug material can be deduced to be qualitatively similar to the one found in model 3a. Again, increasing D_{plug} leads to less Hastelloy N and subsequently the plug is cooled less, leading to a greater portion of the plug to be molten. This relation becomes even more evident by examining the results of figure 4.19.

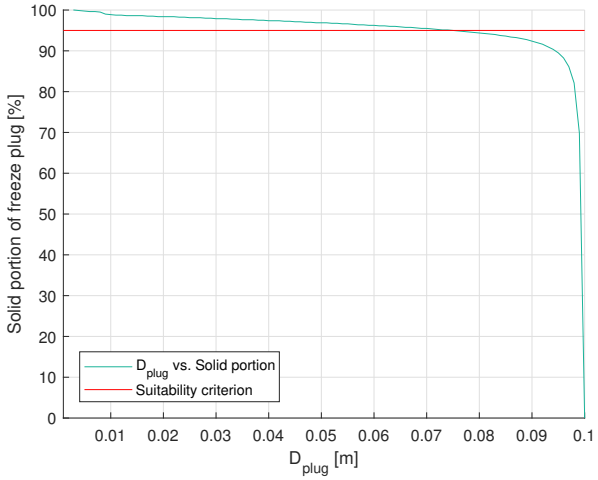

Figure 4.19: Relation of D_{plug} and percentage solid CsCl.

The figure clearly displays the negative correlation that was examined before in figure 4.16. The qualitative behaviour of the steep transition from a low to a high gradient around a D_{plug} of 0.095 m is also similar to the analysis with the $k-\epsilon$ model. The value of D_{plug} for which the 95% criterion

is reached is equal to 0.075 m. The translation as to the total cooling power P_{total} was performed identically to the one in model 3a. Figure 4.20 presents the result.

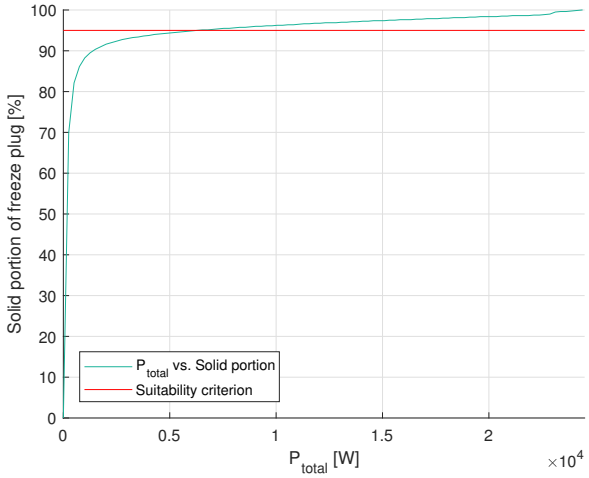

Figure 4.20: Model 3b relation between P_{total} and percentage solid CsCl.

From the figure it is learned that the 95% threshold is attained for a total cooling power P_{total} of 6.28 kW.
The geometry is also influenced by another parameter though. The distance between two adjacent freeze plugs F_{plug} directly influences the configuration of the plug module, both in the amount of Hastelloy N between plugs, but also in the amount of plugs in the module. With a smaller F_{plug}, the plug module can hold more freeze plugs.

4.3.3 Model 4a: Adjacent plug distance influence with $k - \epsilon$ module

Investigating the adjacent plug distance F_{plug} requires a different strategy than used in the previous models, because of the relevant constraints. As was done in models 2a and 2b, the plug diameter is fixed at 0.04 m, making up the first constraint. F_{plug} should in any case not decrease below 0.04 m, because it would cause for adjacent plugs to overlap, since F_{plug} is measured from the center of the adjacent plugs.
When examining figure 4.14, one could imagine that with decreasing F_{plug}, space opens up for an additional plug of diameter 0.04 m. To ensure realistic conditions, the outer 0.025 cm of the plugs module are not allowed to be occupied by a freeze plug, keeping in mind that the plug module is encased in a alloy draining pipe and needs to be securely attached to it. By imposing these constraints, only a limited number of plug configurations are possible for certain values of F_{plug}.
For a given number of plugs, varying F_{plug} might not pose much of an impact on the percentage of solid CsCl, because the total cooling power remains the same, as the amount of Hastelloy N is not changed. Changing the number of plugs, however, alters the ratio of CsCl to Hastelloy N and is therefore likely to have an impact on the percentage solid freeze plug material. By this reasoning, a valid approach to capturing the influence of F_{plug} on the cooling requirements is to generate some measurements per number of plugs and the according F_{plug}, and then using the curve fitting tool in MATLAB to retrieve the relation of F_{plug} to the percentage solid CsCl.

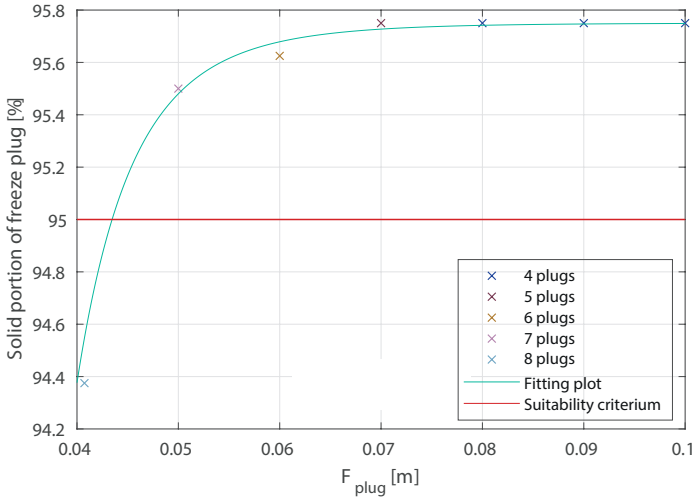

Figure 4.21: Fit of F_{plug} influence on solid portion CsCl, including plug configuration measurements.

From the fit, it becomes clear that increasing the number of plugs does indeed bring about a decrease in percentage of solid CsCl. It is also noted, from the measurements with 4 plugs, that for different values of F_{plug} the portion of solid CsCl does not differ, indicating that the 95% criterion is reached for a plug module with 7 plugs with a plug diameter of 0.04 m or less. The MATLAB script is adopted in Appendix C, containing the exponential fit function and parameters.

4.3.4 Model 4b: Adjacent plug distance influence with Algebraic yPlus module

The results of model 4b were obtained using the same strategy as model 4a. First, separate measurements were made for different number of plugs. Subsequently, the measurements were used to construct a fitting plot, using the curve fitting tool in MATLAB. The outcome of the post-processing is presented in figure 4.22.

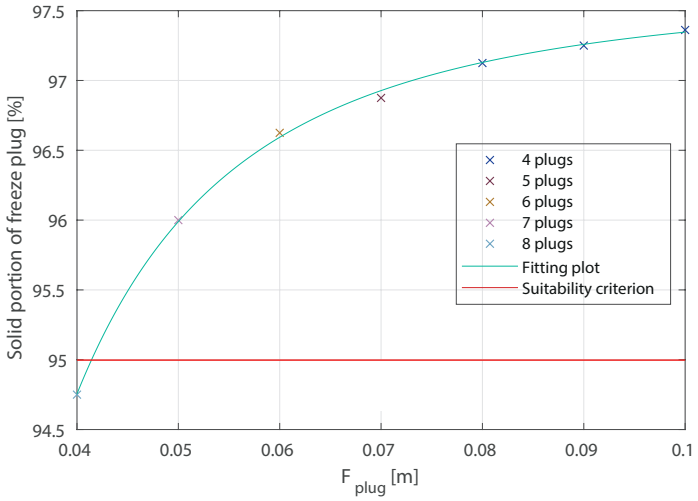

Figure 4.22: Fit of F_{plug} influence on solid portion CsCl, including plug configuration measurements.

Again, it is noted that increasing the number of plugs is the strongest force in influencing the

percentage of solid CsCl and the threshold is reached for 7 plugs or less. It is, however, gathered that increasing F_{plug} for four plugs does pose an influence, albeit a limited one, on the percentage of solid freeze plug material, in contrast to the results of figure 4.21. The reason for this could be that in the probing for the data in COMSOL, the center of the plug that was most downstream was used. With varying F_{plug}, the distance downstream also varies, which could account for the difference in the measurements. While probing for data for model 4a, the center of the most downstream plug was also used, only then the position of the plug was fixed and the position of the other plugs was based off of it, which could explain why the difference did not occur for the measurements in figure 4.21.
To conclude the present section on the geometry influence on the cooling requirements, the results of models 3a, 3b, 4a and 4b are summarized and discussed collectively. The findings will then be translated into an indication for the total cooling power P_{total} for the freeze plug module.

4.3.5 Geometry influence on total cooling power P_{total}

The results of the collective models in section 4.3 on the influence of the plug module geometry on the cooling requirements allow for several summarizing and concluding remarks to be made.

- Since the volumetric cooling power $P_{cooling}$ is exclusively assigned to the Hastelloy N in the plug module, increasing the amount of CsCl, and inevitably decreasing the amount of Hastelloy N, leads to a greater portion of the freeze plug to be molten. This holds true for increasing the amount of CsCl by either increasing plug diameter D_{plug} or by increasing the number of plugs.

- Altering the adjacent plug distance F_{plug} while remaining the number of plugs the same, does not pose a significant influence on the cooling requirements. Figure 4.21 demonstrates that by keeping the position of a plug fixed the percentage solid CsCl does not change with increasing F_{plug}. The temperature distribution in a single freeze plug does therefore not seem to be significantly influenced by the presence of an adjacent freeze plug.

- Models 3a and 3b present a rather steep transition in the influence of D_{plug} on the percentage solid material near a plug diameter of 0.095 m. The same qualitative behaviour of a steep transition is observed when 8 freeze plugs are used in models 4a and 4b. This steep transition is reflected in figures 4.17 and 4.20, from which it becomes clear that with a relatively small cooling power, a large portion of the plug of up to 90 % can be kept solid. To visualise this further, from model 3a it is learned that is requires roughly 6.5 times more total cooling power to cool the plug for 95 % than it takes to cool the plug for 90 %. The reason for this could lie in the fact that the plug module was modelled to be insulated at all sides, except for the interface with the molten salt flow. In other words, cooling the area of the plug near the molten salt flow proves to be difficult, while cooling the lower part of the plug is done with relative ease in the models employed.

- Taking into consideration that the volumetric cooling power used in models 3a and 3b was 2.5 MW/m^3, it makes sense that the resulting plug diameters of 0.061 m and 0.075 m did not break even with the plug diameter of 0.04 m used in model 2. The finding that was striking was that the total cooling powers associated with the new plug diameters were also dissimilar from the ones found in model 2a and 2b. The total cooling powers of model 3a and 3b of 9.81 kW and 6.28 kW respectively were notable smaller than their model 2 counterparts. This might imply that a higher volumetric cooling power cools the plug more efficiently, causing

it to be sufficiently cooled with only a small portion of Hastelloy N present in the plug and resulting in a lower total cooling power needed.

Chapter 5

Conclusions and recommendations

5.1 Conclusions

In chapter 1, the principal aim of this thesis was brought forward, declaring that this thesis is directed at capturing the cooling requirements for a suitable freeze plug module. The most current MSFR design brought forward that the MSFR will feature not one but 16 freeze plug modules, each assigned to a separate draining pipe. The research in this thesis aimed its attention to capturing the cooling requirements for a single freeze plug module under normal operating conditions of the MSFR. The first step to achieving this was to model the molten salt flow in 2D. Concerning the molten salt flow, the following conclusions can be drawn based on the performed research:

- The molten LiF-ThF_4 flow is in the turbulent regime. The Reynolds number associated with the channel flow is 196000, which clearly surpasses the appropriate critical Reynolds number of 1800. Under normal operating conditions, the molten salt flow in the section above the plug has a free flow velocity of 3.2 m/s and the velocity profile is in accordance with a highly turbulent channel flow, with a narrow laminar sublayer and a buffer layer extending around 0.1 mm and 0.2 mm into the channel, respectively.
- In order to model the turbulent flow, two turbulence modules were used, namely the $k-\epsilon$ and Algebraic yPlus modules. The Algebraic yPlus module produces the most accurate cooling requirements. The $k-\epsilon$ module uses wall functions to model the flow near the wall, which resulted in modelling a too high plug surface temperature. The elevated plug surface temperature caused for somewhat higher cooling requirements, which are believed to be less realistic. The cooling requirements produced by the $k-\epsilon$ module were between 18% and 56 % higher than their counterparts produced by the Algebraic yPlus module.
- It was found that under appropriate cooling conditions no solid salt is formed on top of the plug surface. The combination of the narrow laminar sublayer and the low melting temperature of LiF-ThF_4 ensures that sediment is only formed when the plug is cooled disproportionately. The first sediment is formed at a volumetric cooling power that is 4 times greater than necessary.

Now that the molten salt flow characteristics are clarified, the findings on the cooling requirements of the freeze plug can be presented. The research on the cooling requirements was twofold. First a suitable total cooling power was identified for a plug geometry in accordance with previous research. Then the influence of the plug module geometry on the cooling requirements was investigated. The

suitability criterion for the total cooling power used was that the freeze plug material CsCl should be solid for at least 95%. It was found that:

- For a geometry with four plugs per module, a total cooling power of 12.7e3 W and 10.9e3 W per plug module were found for the $k-\epsilon$ and yPlus modules respectively. When assuming a MSFR energy capacity of 1000 MW, cooling all the 16 plug modules would consume 0.02% and 0.0172% of the total energy production. These values were obtained by using a volumetric cooling power of 2.1 MW/m^3 and 1.8 MW/m^3.
- Since the volumetric cooling power is assigned homogeneously to the Hastelloy N in the plug module, decreasing the amount of Hastelloy N means that the total cooling power decreases. The total cooling power subsequently decreased by increasing the plug diameter or by increasing the number of plugs, causing a greater portion of the plug to melt.
- It is, however observed that for higher volumetric cooling powers, the plug is still appropriately cooled for disproportionately smaller Hastelloy N sections in the plug. This results in a lower total cooling power. It was found that for a volumetric cooling power of 2.5 MW/m^3 a total cooling power per plug module of 9.81 kW and 6.28 kW were obtained for the $k-\epsilon$ and yPlus modules. These cooling powers would amount to using 0.015% and 0.010% of the assumed total MSFR energy capacity for cooling all the 16 plugs.
- Varying the adjacent plug distance did not pose an influence on the cooling requirements. Increasing the number of plugs, and consequently decreasing the amount of Hastelloy N, did exert an impact on the requirements.

The resulting values of the total cooling powers are desirable in the sense that the energy needed to cool all freeze plugs makes up no significant portion of the total energy capacity. The findings on the molten salt flow not being considerably influenced are also advantageous: jeopardising the flow conditions of the molten salt by cooling the plugs would have posed significant challenges to the feasibility of a freeze plug module. Still, extended research in several avenues of the freeze plug module is needed to affirm the results of this thesis and to expand on them.

5.2 Recommendations

In the current work, several assumptions were made to perform the research, of which the most notable perhapd is the 2 dimensional geometry in the COMSOL models, among other. As such, during conducting the research, several new research opportunities arose, which will be listed below.

- *Modelling the 3D geometry.*
  As mentioned, all COMSOL models use a 2D representation for their simulations. Since it concerns a stationary situation and the flow is fully developed, modelling the flow characteristics should be fairly accurate for a channel flow. In the actual reactor design, the molten salt flow goed through a closed duct while traversing the plug surface. This surely impacts the cooling requirements, so additional research into the 3D geometry is advised.
- *Implementing realistic cooling solutions.*
  The volumetric cooling power $P_{cooling}$ is homogeneously assigned to the Hastelloy N in the present work. Realistic cooling systems with a water or air flow do not cool the plug module homogeneously, but rather perform more local cooling. The suitable cooling solutions and their implications and limitations could be a focal point for further research.

- *Including the bottom plug surface.*
  The bottom surface of the freeze plug module in this thesis is modelled to be thermally insulated. In reality, the bottom surface borders on the open draining pipe, so heat transfer is surely taking place over the surface, so it could be included in future models.

- *Finding optimal plug module configuration.*
  In the present work it is recognised that a more effective cooling configuration can be reached by increasing the volumetric cooling power $P_{cooling}$ and decreasing the amount of Hastelloy N in the freeze plug module. The benefits are twofold. First, the total cooling power goes down because the plug is cooled more efficiently and secondly, the freeze plug diameter is increased, ensuring faster draining times in case of an emergency. Figuring out the optimal configuration could be an interesting topic for further research.

Bibliography

[1] World-nuclear.org. (2017). Generation IV Nuclear Reactors: WNA - World Nuclear Association. [online] Available at: http://www.world-nuclear.org/information-library/nuclear-fuel-cycle/nuclear-power-reactors/generation-iv-nuclear-reactors.aspx [Accessed 26 Sep. 2017].

[2] SAMOFAR. (2017). Project - SAMOFAR. [online] Available at: http://samofar.eu/project/ [Accessed 8 Dec. 2017].

[3] Serp, J., Allibert, M., Beneš, O., Delpech, S., Feynberg, O., Ghetta, V., Heuer, D., Holcomb, D., Ignatiev, V., Kloosterman, J., Luzzi, L., Merle-Lucotte, E., Uhlíř, J., Yoshioka, R. and Zhimin, D. (2017). The molten salt reactor (MSR) in generation IV: Overview and perspectives.

[4] V. Ghetta, J. Giraud, P. Rubiolo, M. Tano-Retamales (2017). MSFR Fuel Salt Conditions During Typical Draining Transients. Version 1, Deliverable D3.1, SAMOFAR European project, Grant number: 661891, 2015.

[5] S. Wang, M. Massone, A. Rineiski and E. Merle-Lucotte. Analytical Investigation of the Draining System for a Molten Salt Fast Reactor. Institute for Nuclear and Energy Technologies (IKET), Karlsruhe Institute of Technology (KIT) and Université Grenoble Alpes (2016).

[6] P. Swaroop, Design of a Freeze Plug for the Molten Salt Reactor (MSR), msc. thesis, Delft university of Technology (2015).

[7] F. van Tuyll, A new design for the safety plug in a Molten Salt Fast Reactor, bsc. thesis, Delft University of Technology (2016).

[8] A. Makkinje, Design of a Freeze Plug Grate, bsc. thesis, Delft University of Technology (2016).

[9] F. Deurvorst, Design of Cooling Fins on the Freeze Plug, bsc. thesis, Delft University of Technology (2016).

[10] M. Robertson, DEVELOPMENT OF FREEZE VALVE FOR USE IN THE MSRE. In: (1962).

[11] R.C. Robertson, MSRE DESIGN AND OPERATIONS REPORT. PART I. DESCRIPTION OF REACTOR DESIGN. Tech. rep. Oak Ridge National Lab., Tenn., 1965.

[12] V. Ignatiev, O. Feynberg, A. Merzlyakov, A. Surenkov, A. Zagnitko, V. Afonichkin, A. Bovet, V. Khokhlov, V. Subbotin, R. Fazilov, M. Gordeev, A. Panov and A. Toropov (2012). Progress in development of MOSART concept with Th support.

[13] E. Capelli O. Beneš, M. Beilmann and R.J.M. Konings (2012). Thermodynamic investigation of the LiF–ThF4 system. In: The Journal of Chemical Thermodynamics 58 (2013), pp. 110-116.

[14] H. van den Akker and R. Mudde. *Fysische Transportverschijnselen.* Delft Academic Press, fourth edition, 2014.

[15] Stephen B. Pope. *Turbulent Flows.* Cambridge University Press, first edition, 2000.

[16] David C. Wilcox. *Turbulence Modeling for CFD.* DCW Industries, Inc., second edition, 1994.

[17] COMSOL. version 5.3 2016

[18] M. Zijlema. Computational modeling of turbulent flow in general domains, PhD. thesis, Delft University of Technology (1996).

[19] Computationalfluiddynamics.com.au (2017). Selection of wall functions and Y+. [online] Available at: https://www.computationalfluiddynamics.com.au/turbulence-part-3-selection-of-wall-functions-and-y-to-best-capture-the-turbulent-boundary-layer/ [Accessed 10-12-2017].

[20] R. Shankar Subramannian. Heat transfer in flow through conduits. Department of Chemical and Biomolecular Engineering, Clarkson University.

[21] MATLAB. version (R2016b). The MathWorks Inc., Natick, Massachusetts, 2017

[22] Adobe illustrator CC 2017 21.0.0 (64-bit).

Appendix A

Graphs

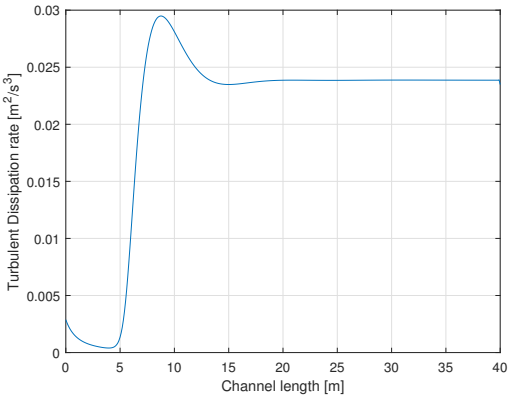

(a) Downstream ϵ value.

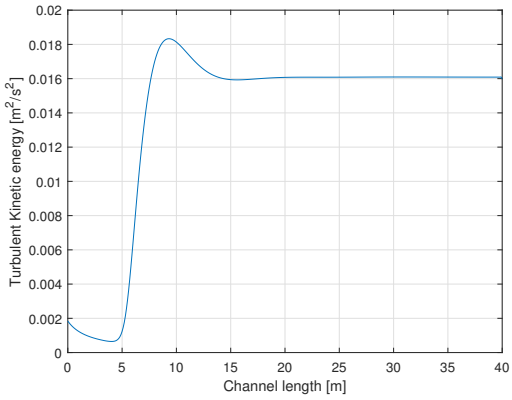

(b) Downstream k value.

Figure A.1: Downstream turbulence variables in the middle of the channel at y=0.075 m

Appendix B

MATLAB scripts

B.1 Plotting the velocity profile

```
%% Berekening Profielen model 1
clear all;
close all;
clc;

%% Data+Variabelen
x=[0:0.001:0.15];
y=[0:0.1:40];
C1 = readtable('Vel_profile.csv');
Data1 = C1;
Data1= table2array(Data1);

C2 = readtable('k_profile.csv');
Data2 = C2;
Data2= table2array(Data2);

C3 = readtable('ep_profile.csv');
Data3 = C3;
Data3= table2array(Data3);

C4 = readtable('Streamwise_vel.csv');
Data4 = C4;
Data4= table2array(Data4);

C5 = readtable('Streamwise_k.csv');
Data5 = C5;
Data5= table2array(Data5);
Data5=Data5(152:552);

C6 = readtable('Streamwise_eps.csv');
Data6 = C6;
Data6= table2array(Data6);
```

```
33
34
35
36
37 %% Plot
38
39 width = 6;       %Width in inches
40 height = 4;      %Height in inches
41 alw = 0.75;      %Axes Line Width
42 fsz = 11;        %Fontsize
43 lw = 0.4;        %Line Width
44 msz = 10;        %Marker Size
45
46
47 pos =get(gcf,'Position');
48 set(gcf,'Position', [pos(1) pos(2) width*100, height*100]);    %<-
     Setsize
49 set(gca,'FontSize',fsz,'LineWidth', alw) ;%<?-Setproperties
50 plot(Data1,x,'LineWidth',lw ,'MarkerSize',msz) ;
51 xlabel('Flow velocity [m/s]') ;
52 ylabel( 'Channel height [m]');
53 axis([0 4 0 0.15])
54 grid on
55 figure
56 plot(Data2,x,'LineWidth',lw ,'MarkerSize',msz) ;
57 xlabel('Turbulent Kinetic Energy [m^2/s^2]') ;
58 ylabel('Channel height [m]');
59 grid on
60 figure
61 plot(Data3,x,'LineWidth',lw ,'MarkerSize',msz) ;
62 xlabel('Turbulent Dissipation rate [m^2/s^3]') ;
63 ylabel('Channel height [m]');
64 grid on
65 figure
66 plot(y,Data4,'LineWidth',lw ,'MarkerSize',msz) ;
67 ylabel('Flow velocity [m/s]') ;
68 xlabel('Channel length [m]');
69 grid on
70 figure
71 plot(y,Data5,'LineWidth',lw ,'MarkerSize',msz) ;
72 ylabel('Turbulent Kinetic energy [m^2/s^2]') ;
73 xlabel('Channel length [m]');
74 grid on
75 figure
76 plot(y,Data6,'LineWidth',lw ,'MarkerSize',msz) ;
77 ylabel('Turbulent Dissipation rate [m^2/s^3]') ;
78 xlabel('Channel length [m]');
79 grid on
```

B.2 Near-wall investigation

```
%% Plot model Near Wall 2a
clear all;
close all;
clc;

% Data+Variabelen
x=[-7e-4:1e-5:7e-4];
C1 = readtable('BL_Hast.csv');
Data1 = C1;
Data1= table2array(Data1);

C2 = readtable('BL_Hast_2.csv');
Data2 = C2;
Data2= table2array(Data2);

%% PLOT

width = 6;      %Width in inches
height = 4;     %Height in inches
alw = 0.75;     %Axes Line Width
fsz = 11;       %Fontsize
lw = 0.4;       %Line Width
msz = 10;       %Marker Size

y= ones(1,71).*918;
z= ones(1,71).*848;

hold on


plot(x,Data1,'LineWidth',lw ,'MarkerSize',msz) ;
xlabel('Arc length [m]') ;
ylabel( 'Temperature [K]');
axis([-3.5e-4 ,3.5e-4 800 1000]);
grid on

plot(x(1:71),y,'k',x(71:141),z,'r');
legend('Near-wall T profile','T_{melt} CsCl','T_{melt} LiF-ThF_{4}','
    Location','SouthWest');

hold off
figure
hold on
plot(x,Data2,'LineWidth',lw ,'MarkerSize',msz) ;
xlabel('Arc length [m]') ;
```

```
ylabel( 'Temperature [K]');
axis([-3.5e-4 ,3.5e-4 800 1000]);
grid on

plot(x(1:71),y,'k',x(71:141),z,'r');
legend('Near-wall T profile','T_{melt} CsCl','T_{melt} LiF-ThF_{4}','
    Location','SouthWest');
hold off
```

B.3 Percentage plot generation

```
% PERC PLOT 3A
close all
clear all
clc

%DATA + VARIABELEN

C1 = readtable('3a_perc_2.csv');
Data1 = C1(1:99,2:1602);
Data1= table2array(Data1);
xt=[0.001:0.001:0.1];
Ahast= 0.032 - 4.*0.08.*xt;
Ptot = Ahast.*2.5e6;
y=zeros(99,1601);

for k=1:99
    for l=1:1601
        if Data1(k,l)<=918
            y(k,l)=1;

        end
    end
end
x=transpose(y);
sl=0.0001.*sum(x);
p=(sl./0.08)*100;
pt=[p 0];
yt=ones(1,100).*95;

%% GENEREER PLOT

width = 6;      %Width in inches
height = 4;     %Height in inches
alw = 0.75;     %Axes Line Width
fsz = 11;       %Fontsize
lw = 0.6;       %Line Width
msz = 10;       %Marker Size
```

```
38
39 hold on
40
41
42 plot(xt,pt,'Color',[0.1 0.7 0.6],'LineWidth',lw ,'MarkerSize',msz) ;
43 xlabel('D_{plug} [m]') ;
44 ylabel( 'Solid portion of freeze plug [%]');
45 axis([0.001 0.1 0 100]);
46 grid on
47 plot(xt,yt,'r');
48 legend('D_{plug} vs. Solid portion','Suitability criterion','Location',
       'SouthWest')
49
50 hold off
51
52 % hold on
53 % plot(xt,yt,'r-')
54 % plot(xt,pt)
55 % hold off
```

Appendix C

Model log

C.1 COMSOL model log

Table C.1: Overview of some of the COMSOL models.

Datum	2D/3D	Mesh density	P0 (e6)	Runtime [hrs]
20-okt	3D	C5	4	0
23-okt	3D	C1	4	0
23-okt	3D	C1	4	0
23-okt	3D	C1	4	0
23-okt	3D	C2	4	9,5
23-okt	3D	C2	4	15,5
23-okt	3D	C4	6	9,16
23-okt	3D	C4	6	0
23-okt	3D	C4	(2E6;2E6;10E6)	13,3
23-okt	3D	C4	4	3,16
23-okt	3D	C4	4	0,6
24-okt	3D	C1	4	0
24-okt	3D	C1	4	0
24-okt	3D	C1	4	0
24-okt	3D	C1	4	0
24-okt	3D	C1	4	0
24-okt	3D	C1	4	0
24-okt	3D	C2	4	40
24-okt	3D	C2	4	40
24-okt	3D	C2	4	40
24-okt	3D	C2	4	40
24-okt	3D	C3	4	3,5
25-okt	3D	C1	2	0,16
25-okt	3D	C1	2	0,16
25-okt	3D	C1	(1E2,1E3,1E4,1E5)	0,5
25-okt	3D	C1	(1E2,1E3,1E4,1E5)	1,25
25-okt	3D	C1	1,00E+04	0,25

Table C.2: Overview of COMSOL models 2

Datum	2D/3D	Mesh density	P0 (e6)	Runtime [hrs]
26-okt	3D	C1	(5E4,0.5E4,15E4)	2,75
26-okt	3D	C3	9,00E+04	3,5
26-okt	3D	C4	9,00E+04	13,1
27-okt	3D	C1	(1E4,0.5E4,5E4)	1,16
27-okt	3D	C1	4,00E+04	0,75
28-okt	3D	C1	2	0,13
5-nov	3D	C5	9,00E+04	35
7-nov	3D	C2	(1E4,0.5E4,5E4)	3,4
7-nov	3D	C3	(1E4,0.5E4,5E4)	4,44
7-nov	3D	C4	(1E4,0.5E4,5E4)	6,164
7-nov	3D	C5	(1E4,0.5E4,5E4)	16,5
8-nov	3D	C1	3,00E+04	3,33
8-nov	3D	C2	3,00E+04	9,44
8-nov	3D	C3	3,00E+04	13,5
8-nov	3D	C4	3,00E+04	19,4
8-nov	3D	C4	3,00E+04	35,5
9-nov	3D	C1	3,00E+04	0
9-nov	3D	C1	3,00E+04	0
9-nov	3D	C2	3,00E+04	0

Table C.3: Overview of COMSOL models 3

Datum	2D/3D	Mesh density	P0 (e6)	Runtime [hrs]
10-nov	2D	C1	-	0,24
10-nov	2D	C4	-	2,08
10-nov	2D	C1	3,00E+04	0,2
10-nov	2D	C4	3,00E+04	1,85
10-nov	2D	C4	3,00E+04	1,4
13-nov	2D	C1	3,00E+04	0,2
13-nov	2D	C4	3,00E+04	1
13-nov	2D	C1	3,00E+04	0,5
13-nov	2D	C1	3,00E+04	0,25
13-nov	2D	C1	3,00E+04	0,2
13-nov	2D	C1	3,00E+04	0,25
13-nov	2D	C1	3,00E+04	0,3
13-nov	2D	C4	3,00E+04	2,4
13-nov	2D	C4	3,00E+04	2,1
21-nov	2D	C4	3,00E+04	2,7
21-nov	2D	C4	3,00E+04	2,3